

Review

# Bubbles Management for Enhanced Catalytic Water Splitting Performance

Zheng Zhang <sup>1,†</sup>, Chen Gu <sup>1,†</sup>, Kun Wang <sup>1</sup>, Haoxuan Yu <sup>1</sup>, Jiaxuan Qiu <sup>1</sup>, Shiyan Wang <sup>1</sup>, Longlu Wang <sup>1,\*</sup>  and Dafeng Yan <sup>2,\*</sup>

<sup>1</sup> College of Electronic and Optical Engineering & College of Flexible Electronics (Future Technology), Nanjing University of Posts & Telecommunications (NJUPT), 9 Wenyuan, Nanjing 210023, China

<sup>2</sup> College of Chemistry and Chemical Engineering, Hubei University, Wuhan 430062, China

\* Correspondence: wanglonglu@njupt.edu.cn (L.W.); dafengyan@hubu.edu.cn (D.Y.)

† These authors contributed equally to this work.

**Abstract:** Water splitting is widely acknowledged as an efficient method for hydrogen production. In recent years, significant research efforts have been directed towards developing cost-effective electrocatalysts. However, the management of bubbles formed on the electrode surface during electrolysis has been largely overlooked. These bubbles can impede the active sites, resulting in decreased catalytic performance and stability, especially at high current densities. Consequently, this impediment affects the energy conversion efficiency of water splitting. To address these challenges, this review offers a comprehensive overview of advanced strategies aimed at improving catalytic performance and mitigating the obstructive effects of bubbles in water splitting. These strategies primarily involve the utilization of experimental apparatus to observe bubble-growth behavior, encompassing nucleation, growth, and detachment stages. Moreover, the review examines factors influencing bubble formation, considering both mechanical behaviors and internal factors. Additionally, the design of efficient water-splitting catalysts is discussed, focusing on modifying electrode-surface characteristics. Finally, the review concludes by summarizing the potential of bubble management in large-scale industrial hydrogen production and identifying future directions for achieving efficient hydrogen production.



**Citation:** Zhang, Z.; Gu, C.; Wang, K.; Yu, H.; Qiu, J.; Wang, S.; Wang, L.; Yan, D. Bubbles Management for Enhanced Catalytic Water Splitting Performance. *Catalysts* **2024**, *14*, 254. <https://doi.org/10.3390/catal14040254>

Academic Editor: Bruno Fabre

Received: 18 March 2024

Revised: 7 April 2024

Accepted: 8 April 2024

Published: 11 April 2024



**Copyright:** © 2024 by the authors. Licensee MDPI, Basel, Switzerland. This article is an open access article distributed under the terms and conditions of the Creative Commons Attribution (CC BY) license (<https://creativecommons.org/licenses/by/4.0/>).

## 1. Introduction

With increasing global concern over climate change and environmental degradation, there is a growing shift away from traditional fossil fuels towards cleaner and renewable energy sources [1–3]. Hydrogen, as a renewable and clean energy alternative, holds significant promise in replacing fossil fuels [4,5]. Water splitting emerges as one of the most environmentally friendly and sustainable methods for hydrogen production. However, the efficiency of water splitting crucially depends on the development of electrocatalytic materials [6–8]. The core of water electrolysis lies in the electrochemical reactions occurring at the electrode surfaces. At the cathode, water is reduced to hydrogen gas, while at the anode, water is oxidized to oxygen gas [9]. These reactions lead to the formation of hydrogen and oxygen gases at the electrode surfaces, which are eventually released in the form of bubbles. When gases diffuse and accumulate near the electrode surfaces in the electrolyte, initial nucleation of bubbles occurs [10–12]. Once bubbles form, they continue to grow within the electrolyte until they reach a sufficient size to be released from the electrode surfaces. The growth rate of bubbles depends on gas-diffusion rates, electrolyte-flow conditions, and electrode-surface properties. When bubbles reach a critical size, they are released from the electrode surfaces and rise to the electrolyte surface due to buoyancy. Upon release into the electrolyte, bubbles gradually dissolve as a result of gas diffusion [13–16].

The surface characteristics of electrodes play a pivotal role in the formation and release of bubbles during electrolysis, particularly under high current density conditions [17,18]. The accumulation of bubbles on electrode surfaces hinders active sites, thereby impacting catalytic performance and stability [19]. Bubbles can impede the mass transfer of reactants to the electrode surface, especially when they form a gas film [20–22]. Additionally, the formation of large bubbles or air pockets in the electrolyte disrupts the uniformity of the electrolyte solution. Bubbles can hinder effective contact between electrodes and electrolytes during electrolysis, leading to a decrease in the rate of electrochemical reactions and thus affecting water-splitting efficiency. Additionally, bubbles may cause instability in gas-liquid two-phase flow, resulting in uneven distribution of the flow field inside the reactor, thereby affecting the performance and stability of the reactor. This uneven distribution can lead to localized changes in reactant concentration and pH, thereby affecting the kinetics of electrochemical reactions [23–27]. Moreover, bubble growth and detachment can lead to the loss of active species, further compromising electrocatalyst performance.

In recent years, research efforts have increasingly focused on developing electrocatalysts with reduced bubble adhesion. There are several strategies to reduce bubble adhesion. One approach is to modify the surface properties of electrocatalysts to alleviate bubble adhesion. This can be achieved by applying hydrophobic or superhydrophobic coatings to the surface [28]. These coatings exert a repulsive force on bubbles, preventing them from adhering to the electrode surface. Additionally, surface-roughening techniques, such as electrodeposition or etching, can be used to create micro or nanostructures, thereby minimizing the contact area with bubbles [29–32]. Another strategy involves carefully selecting electrode materials with intrinsic properties that deter bubble attachment. For instance, materials like graphene and carbon nanotubes exhibit low surface energy and high conductivity, making them less prone to bubble adhesion [33–36]. Similarly, transition metal oxides and sulfides are being investigated for their fouling-resistant properties, which can reduce bubble adhesion. Furthermore, designing nanoscale features on the electrode surface, such as nanopores or nanowires, provides an effective means to reduce bubble adhesion. These nanostructures form a barrier that limits bubble attachment and facilitates their detachment from the electrode surface [37,38]. However, synthesized electrocatalysts' surface properties under high current density have not yet met the rigorous requirements for large-scale practical applications [39,40]. Improving the electrochemical performance of nanostructured electrocatalysts under high current density and implementing effective strategies to address bubble accumulation on electrode surfaces are imperative to maintaining catalyst activity.

In this review, we discuss intrinsic methods for observing bubble-growth behavior, such as the high-frequency impedance method and the time-varying potential method. We also examine the influence of physical, mechanical, and internal factors on bubbles, and systematically discuss the impact of altering catalyst surface characteristics on bubble detachment, including the design of electrocatalysts with superhydrophobicity and superhydrophilicity. Additionally, centralized bubble separation and transportation strategies are summarized, followed by insights into future development directions. This review contributes to advancing strategies for efficient bubble management in water electrolysis, thereby facilitating large-scale hydrogen production.

## 2. Bubble-Behavior Monitoring

The bubbles formed during the water-splitting process significantly impact the efficiency and performance of electrochemical reactions. Adverse effects of bubbles, such as excessive overpotential and unstable currents, can result in energy efficiency losses, blockage of active sites on electrode surfaces due to bubble adhesion, and physical degradation of catalysts caused by increased bubble size leading to tensile forces [41]. The lack of real-time bubble detection presents a significant challenge to improving electrolysis efficiency. Therefore, the development of effective bubble-characterization strategies is crucial for optimizing the electrolysis process. Experimental strategies include direct

observation of bubble formation, growth, and detachment on electrode surfaces using techniques such as high-speed imaging, scanning electron microscopy (SEM), and atomic force microscopy (AFM) [42]. In situ monitoring methods, such as impedance monitoring, in situ monitoring, and current monitoring, can provide real-time data on bubble dynamics during electrolysis. Undoubtedly, these monitoring techniques exhibit limitations. High-frequency impedance bubble monitoring, for instance, may lack the sensitivity required to detect bubbles accurately, potentially resulting in the oversight of tiny bubbles. Furthermore, environmental factors can significantly interfere with the precision and stability of high-frequency impedance bubble monitoring [43–45]. In microfluidic systems, the rapid movement and dispersion of bubbles due to the high speed of liquid flow pose additional challenges to monitoring efforts. Additionally, the high cost associated with the preparation and operation of microfluidic reactors restricts their widespread adoption in practical applications, necessitating a high level of technical expertise and operational experience to operate them effectively. The effectiveness of monitoring results obtained through chronopotentiometry is heavily reliant on electrode performance, which may vary under different conditions [46,47]. Similarly, SPRi technology, while promising, typically requires some time to capture images and perform analysis, rendering it difficult to monitor bubbles in instantaneous or rapidly dynamic processes, particularly in scenarios with high bubble concentrations or rapid dynamic changes. By comprehensively analyzing the advantages and disadvantages of various monitoring technologies, it is imperative to select monitoring techniques judiciously to enhance monitoring efficiency and ensure reliable results [48]. By integrating experimental and theoretical methods, a comprehensive understanding of the dynamic characteristics of bubbles in water electrolysis can be achieved, facilitating the development of efficient electrolysis systems for hydrogen production.

### 2.1. Operando Monitoring by Single High-Frequency Impedance

The development of efficient electrolysis systems for hydrogen production necessitates a comprehensive understanding of bubble dynamics. Traditional characterization methods, such as visual observation and gas analysis, have limitations in providing real-time quantitative data on bubble evolution [49,50]. High-frequency impedance spectroscopy offers unique advantages in this regard, allowing for continuous monitoring of bubble behavior. The formation of bubbles during water electrolysis alters the electrochemical-reaction conditions at the electrode surface, thereby affecting the overall electrochemical behavior of the electrolysis process and causing changes in system impedance. Through the analysis of impedance spectra, information regarding bubble size, distribution, and dynamics can be extracted. High-frequency impedance spectroscopy (HFIS) provides a powerful and versatile method for characterizing bubble behavior in water electrolysis. It enables real-time quantitative analysis of bubble dynamics and is an important tool for advancing the development of efficient hydrogen-production technologies.

As shown in Figure 1a, the amplitude of resistance fluctuation indicates the non-periodic impact of bubble evolution on the electrode surface. It is observed that a higher amplitude correlates with an increased quantity of bubbles, accompanied by a decrease in the rates of both growth and detachment from the electrode surface. The behavior of these bubbles is influenced by the electrode structure. Additionally, the nanostructured surface of NF exhibits a multi-directional hierarchical structure, which plays a key role in creating gas-repellent surfaces and manipulating bubbles. The effect of surface wetting and anisotropic morphology on gas-bubble evolution (GBE) was monitored by single-frequency impedance [51]. With desirable super-wettability,  $\text{Ni(OH)}_2@\text{N-NiC}/\text{NF}$  heterogeneous layered nanostructured electrodes showed significantly improved alkaline hydrogen evolution reaction (HER) performance (Figure 1b). Subsequently, investigations were conducted into the release rate of bubbles and the quantity of bubbles generated per unit time from different electrodes. As depicted in Figure 1c,d, bubbles on the three-dimensional surface of  $\text{Ni(OH)}_2@\text{N-NiC}/\text{NF}$  disperse rapidly, whereas there was no apparent bubble dispersion during the early stages of HER for  $\text{Ni(OH)}_2/\text{NF}$  at low and medium potentials. The number

of bubbles captured per unit time from the  $\text{Ni(OH)}_2@\text{N-NiC}/\text{NF}$  electrode significantly exceeds that of the  $\text{Ni(OH)}_2/\text{NF}$  electrode, as shown in Figure 1e,f. Figure 1g shows a significant reduction in dynamic resistance changes for  $\text{Ni(OH)}_2@\text{N-NiC}/\text{NF}$  at a fixed 20 kHz single-frequency impedance and a current density of  $-100 \text{ mA cm}^{-2}$ . In order to validate the functionality of the single high-frequency impedance for bubble management during the HER process, electrochemical monitoring of GBE was further investigated in an anion-exchange membrane (AEM) water electrolyte (Figure 1h). The method of real-time monitoring GBE was studied in an AEM water electrolysis cell setup, as shown in Figure 1i. In conclusion, tracking dynamic resistance changes at the optimal high-frequency with minimal phase provides a universal alternative approach for operational GBE monitoring in water-electrolysis processes. This method of monitoring GBE is particularly suitable for practical water electrolysis applications, where optical visualization may be limited, and can aid in optimizing electrode performance and stability.

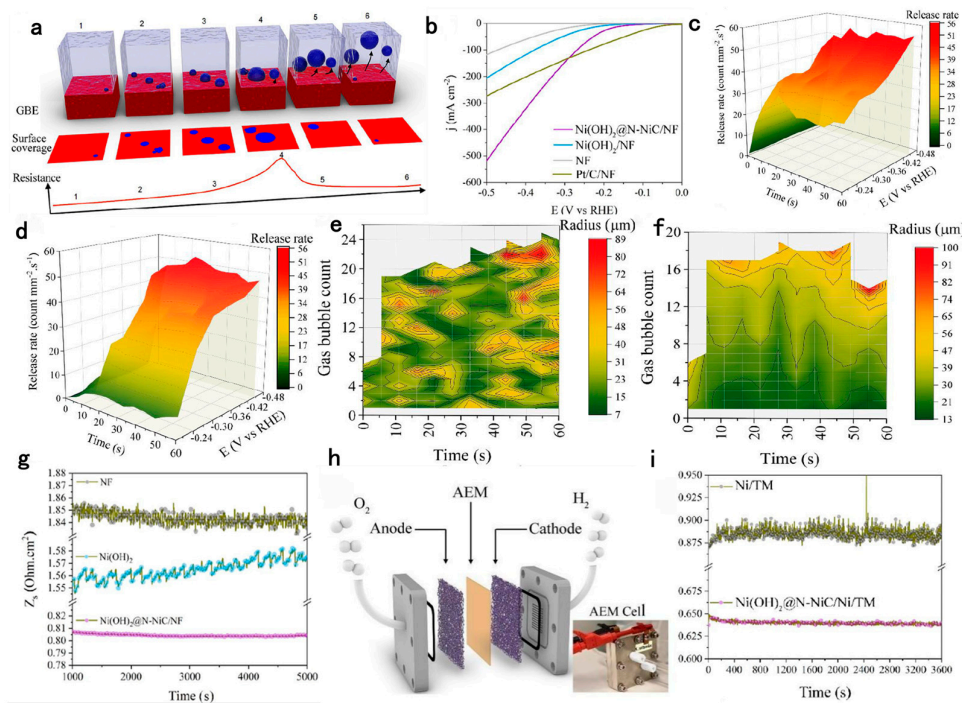


**Figure 1.** (a) Schematic representation of dynamic resistance variation via single frequency impedance. (b) HER polarization curves without ohmic resistance compensation. (c)  $\text{Ni(OH)}_2@\text{N-NiC}/\text{NF}$ . (d)  $\text{Ni(OH)}_2/\text{NF}$ . Contour plots at 0.455V vs. reversible hydrogen electrode (RHE) for. (e)  $\text{Ni(OH)}_2@\text{N-NiC}/\text{NF}$  and (f)  $\text{Ni(OH)}_2/\text{NF}$ . (g) Dynamic resistance variation. (h) Schematic representation and (i) photograph of an AEM water electrolyzer. Reproduced with permission from [51], © 2023 Royal Society of Chemistry.

## 2.2. Operando Monitoring by Chronopotentiometric

Traditional methods for bubble characterization often lack temporal resolution and may not capture transient events. The timing potential method addresses these limitations by providing time-resolved data on bubble dynamics [52]. This method involves periodically measuring the potential of the working electrode during electrolysis. Changes in potential over time reflect the formation and behavior of bubbles on the electrode surface. By analyzing the timing of potential changes, valuable information about bubble nucleation, growth, and detachment can be obtained [53]. The timing potential method can also be combined with other techniques, such as high-speed imaging, to provide complementary information on bubble characteristics [54]. This method offers a valuable approach for characterizing bubbles in electrolysis processes. Its ability to provide time-resolved data

makes it a powerful tool for advancing the understanding of electrolysis processes and optimizing hydrogen production technologies.

Chronopotentiometry is a technique based on the relationship between current and time. By observing the change of current with time, information related to the kinetics of electrochemical reactions can be obtained. Chaewon Song et al. successfully synthesized fibrous tubular  $\text{Ru}_x\text{CrO}_{1-x}$  by electrostatic spinning and optimized calcination atmosphere condition steps, demonstrating excellent catalytic activity and OER durability over a wide range of pH values while maintaining the unique morphology. In particular, the fibrous  $\text{Ru}_x\text{CrO}_{1-x}$  structure in the tube efficiently promotes bubble dynamics by enabling easy detachment of the evolved  $\text{O}_2$  bubbles [55]. The different bubble growth/desorption characteristics of the  $\text{Ru}_x\text{CrO}_{1-x}$ -n series during OER were investigated as shown in Figure 2.  $\text{Ru}/\text{RuO}_2$  exhibited a severe positive potential drift with irregular fluctuations suggesting an irregular  $\text{O}_2$  generation/desorption cycle (Figure 2a).  $\text{Ru}_{x}\text{Cr}_{1-x}\text{O}_y$ -5 (Figure 2b) also showed a positive potential drift, implying that the OER was interrupted by a rather slow  $\text{O}_2$  desorption, where the  $\text{O}_2$  production/desorption cycle was similar to that of  $\text{Ru}_x\text{CrO}_{1-x}$ -50.  $\text{Ru}_x\text{CrO}_{1-x}$ -20 in Figure 2c also shows insignificant overall potential changes, while the potential amplitude is very small at high frequencies. This suggests that at  $\text{Ru}_x\text{Cr}_{1-x}\text{O}_y$ -20,  $\text{O}_2$  bubbles are easily detached and the  $\text{O}_2$  generation/desorption cycle is more regular. Compared to  $\text{Ru}_x\text{Cr}_{1-x}\text{O}_y$ -20,  $\text{Ru}_x\text{Cr}_{1-x}\text{O}_y$ -100 (Figure 2d) showed slower bubble kinetics, resulting in longer bubble generation and desorption cycles. Among the materials tested,  $\text{Ru}_x\text{Cr}_{1-x}\text{O}_y$ -20 demonstrated the most promising characteristics for OER performance, primarily due to its distinctive thin-shell-with-a-core structure. This configuration offered advantages not only in terms of external surface area but also in the interface between the shell and core, enabling efficient oxygen evolution and easy release compared to alternative structures. For bubble monitoring, characteristic changes in the current signal are produced when bubbles are generated or disappear. This is because the formation or disappearance of bubbles alters the mass transfer on the electrode surface, which affects the electrochemical reaction rate and hence the current signal. In conclusion, the chronopotential method, as a sensitive, fast, and reliable technique, has been widely used in the monitoring and research of gas bubbles. Through this method, we can gain a deeper understanding of the process of bubble generation and disappearance.

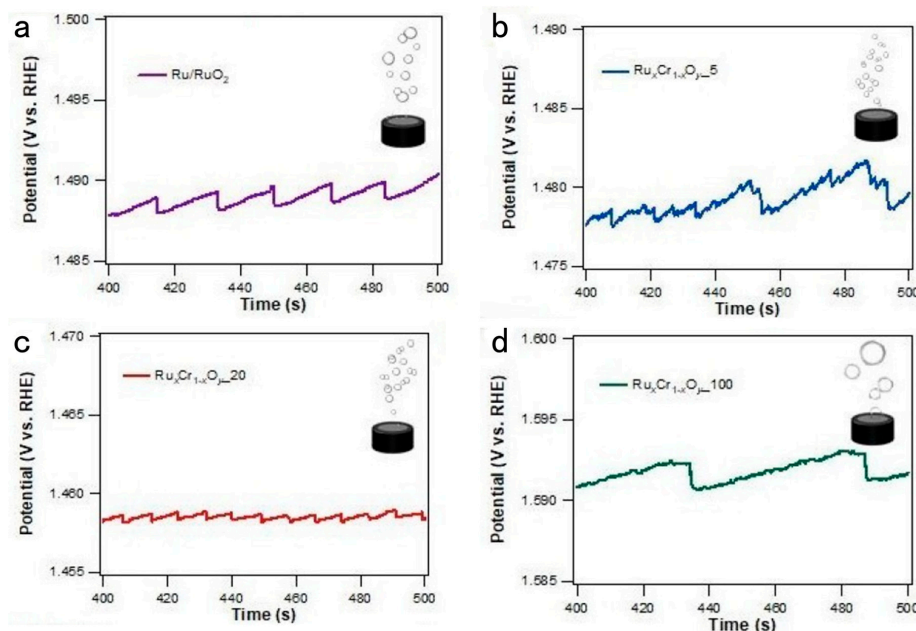


**Figure 2.** Chronopotentiometric monitoring of generated  $\text{O}_2$  gas desorption for (a)  $\text{Ru}/\text{RuO}_2$ , (b)  $\text{Ru}_x\text{Cr}_{1-x}\text{O}_y$ -5, (c)  $\text{Ru}_x\text{Cr}_{1-x}\text{O}_y$ -20, (d)  $\text{Ru}_x\text{Cr}_{1-x}\text{O}_y$ -100 in 1 M KOH aqueous solution. Reproduced with permission from [55], © 2023 Royal Society of Chemistry.

### 2.3. Operando Monitoring by a Microfluidic Reactor

Microfluidic reactors provide a flexible and precise platform for controlling reaction conditions [56,57]. However, the generation and behavior of bubbles in gas-liquid phase reactions have a significant impact on reaction outcomes [58]. Therefore, the development of bubble characterization strategies suitable for microfluidic environments is crucial. Experimental methods for bubble characterization in microfluidic reactors include high-speed imaging, laser scanning confocal microscopy, and flow cytometry [59,60]. These techniques enable real-time observation of bubble formation, evolution, and motion trajectories, providing intuitive data for research. Numerical simulation methods involve establishing mathematical models of microfluidic reactors to simulate gas-liquid phase flow and mass transfer processes, predicting bubble generation and behavior [61,62]. Numerical simulation methods play a pivotal role in the research and design of microfluidic reactors, particularly in understanding the dynamics of gas-liquid phase flow and mass transfer processes, as well as predicting the generation and behavior of bubbles. These mathematical models typically involve solving a set of partial differential equations, such as the Navier–Stokes equations for fluid flow, the convection-diffusion equation for mass transfer, and the Young–Laplace equation for interfacial tension [63,64]. Given the presence of gas-liquid interfaces and bubble formation in microfluidic reactors, accurate modeling of multiphase flow is indispensable. These multiphase flow models elucidate phenomena such as bubble coalescence, breakup, and deformation under different flow conditions. Additionally, numerical simulation can predict the mass transfer rates between the gas and liquid phases, as well as the dynamic behavior of bubbles within microfluidic reactors [65,66]. This approach offers an in-depth understanding of the dynamic behavior of bubbles in microfluidic reactors, supporting experimental design and result interpretation. Bubble characterization strategies in microfluidic reactors comprehensively reveal the generation, evolution, and influencing factors of bubbles [67].

In order to study the two-phase countercurrent mechanism inside the anode PTL and its impact on the performance of PEM electrolytic cells. Xu et al. designed a microfluidic reactor with an oxygen evolution reaction boundary to simulate the through-plane PTL of PEM electrolytic cells (Figure 3a). As depicted in Figure 3b, the evolution of gas phase saturation in the PTL under various current densities is illustrated [68]. With increasing current density, gas saturation rises more rapidly and exhibits a greater frequency of fluctuations. At lower current densities, gas saturation approaches zero. The applied voltage curve and average voltage under different flow rates at a high current density of  $1000 \text{ mA cm}^{-2}$  are shown in Figure 3c. As the flow rate increases, bubbles can be removed quickly with the liquid, which greatly reduces the mass-transfer resistance. As a result, the average voltage between the working electrode and counter electrode decreases with the flow rate. It can be observed from Figure 3d that with an increase in flow rate, the amplitude of voltage fluctuations decreases. At lower flow rates, bubbles tend to move slowly within the flow channel after separating from the PTL, impeding liquid transfer, and resulting in high mass transfer resistance. As the flow rate rises, bubbles are swiftly carried away with the liquid, thereby, significantly reducing mass-transfer resistance. Consequently, owing to the diminished mass-transfer resistance, the average voltage between the working electrode and the counter electrode declines as the flow rate decreases. In conclusion, the microfluidic reactor in conjunction with a high-speed camera enables real-time visualization, quantitative analysis, and insight into bubble-fluid interactions.

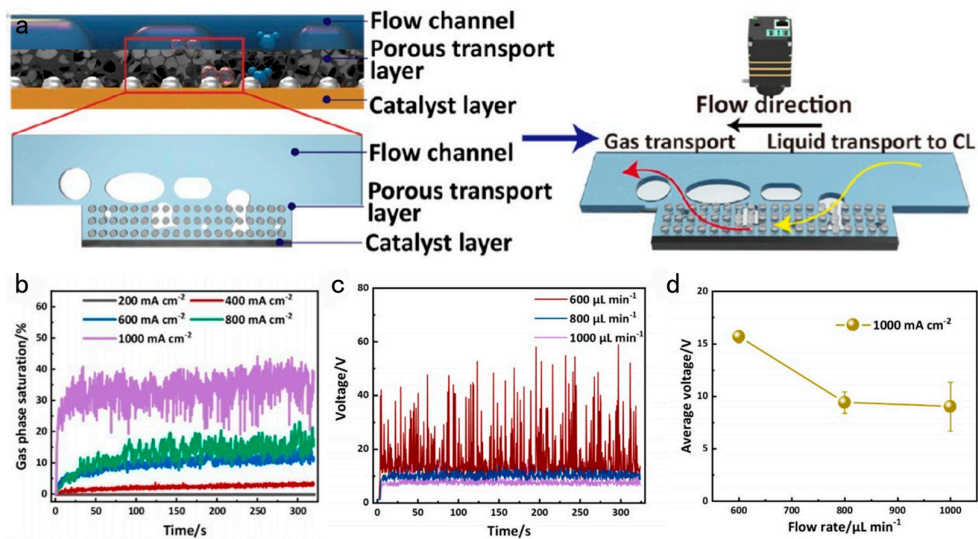


**Figure 3.** (a) Schematic of through-plane view of the porous transport layer (PTL) in the proton exchange membrane (PEM) electrolyzers. (b) The evolution of gas phase saturation in PTL. (c) The applied voltage between the working electrode and the counter electrode under various flow rates at a current density of  $1000 \text{ mA cm}^{-2}$ . (d) The average voltage between the working electrode and the counter electrode under various flow rates. Reproduced with permission from [68], © 2023 Elsevier.

#### 2.4. Operando Monitoring by Electrochemical Surface Plasmon Resonance Imaging

Surface plasmon resonance imaging (SPRI) technology provides a powerful method for monitoring bubbles. This technique relies on the principle of surface plasmon resonance, where changes in the refractive index at the surface of a thin metal film result in alterations in the intensity of reflected light [69]. When applied to bubble detection, SPRI can detect changes in the refractive index caused by the presence of bubbles near the metal surface. SPRI offers several advantages for bubble monitoring. Firstly, it enables real-time and label-free detection of bubbles without the need for invasive probes or markers [70]. Additionally, SPRI provides high sensitivity and spatial resolution, allowing for the precise localization and tracking of bubbles [71]. Furthermore, SPRI can be used to study dynamic processes such as bubble formation, growth, and detachment *in situ*. By leveraging SPRI technology, researchers can gain valuable insights into the behavior of bubbles in various applications, including electrolysis processes [72]. This non-invasive and continuous monitoring approach contributes to a better understanding of bubble dynamics and facilitates the optimization of processes involving bubble formation and detachment.

As shown in Figure 4a, the formation of bubbles during electrolysis usually starts from nanobubbles, which generate high internal pressure and additional overpotentials due to their ultra-small size. Therefore, in this study, the formation and growth process of interfacial nanobubbles in the initial hydrogen production reaction was observed using *in situ* electrochemical surface plasmon resonance imaging combined with atomic force microscopy measurements [73]. As shown in Figure 4b, the electrochemical surface plasmon resonance (EC-SPR) experimental setup was built according to the Kretschmann configuration, where the SPR response (reflectance change) can be obtained from the fully internally reflected light for exploring the behavior of the nanobubbles. As shown in Figure 4c, the coverage of the equilibrium NBs is almost kept at  $7 \pm 1\%$  at different overpotentials. In addition to more aggregation at higher overpotentials, the main reason for the brightening of the SPR image is the change in NB morphology/height. It was found that the growth of nanobubbles starts with pancake-shaped bubbles, followed by an increase in the coverage area, the formation of roughly fixed three-phase boundaries, and an increase in the contact angle and height. However, after equilibrium is reached, the coverage area remains almost constant. Further increase in overpotential leads to an increase in nanobubble curvature (potential shift) as well as an increase in gas outflow rate, i.e., an increase in background

current. In summary, SPRi technology provides a powerful and versatile method for monitoring gas bubbles with real-time, label-free, and high-resolution detection capabilities. It enables researchers to gain insight into the dynamics and behavior of bubbles, facilitating process optimization and the development of new technologies.

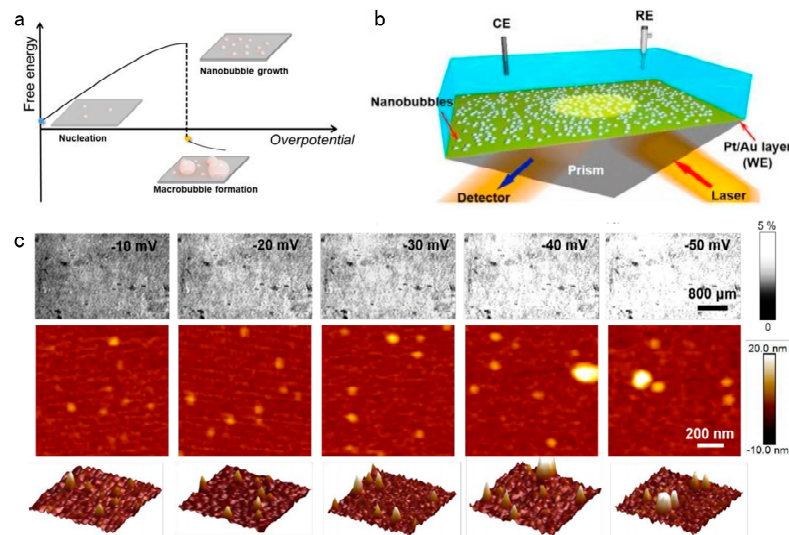


**Figure 4.** (a) Schematic illustration of the relation between the free energy of electrode surface bubbles and the overpotentials during gas phase transformation. (b) Schematic diagram of experimental setup for the electrochemical surface plasmon resonance imaging (EC-SPR). (c) Time-dependent evolution of nanobubble (NB) at an overpotential of 50 mV. Reproduced with permission from [73], © 2023 Royal Society of Chemistry.

### 3. Factors Influencing Bubble Detachment

There are many factors influencing bubble separation during water splitting. Examples include solution Marangoni convection, surface roughness, aerophobicity, hydrophilicity, and mechanical motion. The solution Marangoni effect arises from the ionic concentration gradient formed during the reaction process, which alters the surface tension of the electrolyte, thus affecting the stability and size of the bubbles in the electrolyte, and hence bubble separation [74]. High current density increases the generation of bubbles and their accumulation on the electrode surface, enhancing the interaction and adhesion forces between bubbles, thus affecting bubble separation. The size and morphology of bubbles affect their buoyancy and surface tension in the electrolyte, thereby influencing their stability and separation behavior [75]. The flow rate and direction of the electrolyte affect the movement and detachment of bubbles in the electrolyte. Higher flow rates promote bubble detachment, while lower flow rates may lead to bubble retention and aggregation [76,77]. In summary, bubble detachment is affected by a variety of factors, including electrode surface properties, electrolyte concentration, current density, bubble size and morphology, and flow conditions. A thorough study of the interactions between these factors is required to optimize the water-electrolysis process and improve the efficiency of hydrogen production.

#### 3.1. Solutal Marangoni Effect Determines Bubble Dynamics during Electrocatalytic Hydrogen Evolution

The Marangoni effect refers to the mass or momentum transfer phenomenon caused by a surface-tension gradient. When a surface-tension gradient exists in a liquid, mass or momentum in the liquid will transfer along the surface-tension gradient, leading to flow. In the process of water electrolysis, the Marangoni effect can influence the movement and detachment of bubbles in the electrolyte [78]. Specifically, the Marangoni effect may affect the stability and trajectory of bubbles in the electrolyte, thereby influencing the bubble-detachment process [79]. When a surface-tension gradient exists, for example, due to temperature differences or the presence of surface-active substances, the trajectory of

bubbles may deviate or distort. This alteration in flow patterns can lead to changes in the adhesion force between bubbles and the electrode surface, thereby affecting bubble detachment [80,81]. In summary, the impact of the Marangoni effect on bubble detachment is complex and variable, depending on the strength and direction of the surface-tension gradient and other factors such as temperature changes [82,83]. A deeper understanding of the influence of the Marangoni effect on bubble behavior can help better control bubble formation and detachment in the water-electrolysis process, thereby improving electrolysis efficiency and hydrogen production [84].

In the process of electrochemical water splitting, the coalescence efficiency of microbubbles is related to the Hofmeister series of anions in the electrolyte. As illustrated in Figure 5a, within the  $\text{H}_2\text{SO}_4$  electrolyte, individual bubbles form and detach periodically, whereas in other electrolytes, bubble formation and detachment occur non-periodically. When a sufficiently large overpotential is applied, the periodic evolution of individual  $\text{H}_2$  bubbles can be observed. The overpotential and current for the formation of a single  $\text{H}_2$  gas bubble gradually increase in the order of  $\text{H}_2\text{SO}_4$ ,  $\text{HCl}$ ,  $\text{HNO}_3$ , and  $\text{HClO}_4$  [85]. As shown in Figure 5b, the temperature gradient induces a thermo-Marangoni flow away from the platinum surface area, while the concentration gradient-induced solute Marangoni flow moves away from the platinum surface area with positive surface-tension increments. The concentration gradient-induced solute Marangoni flow counteracts the negative surface-tension increment towards the platinum surface area. The temperature gradient generated by heating can induce a Marangoni flow, and the resulting bubble force moves toward the electrode. As shown in Figure 5c,  $\text{H}_2\text{SO}_4$  and  $\text{HCl}$  were mixed in different proportions, and the higher the surface-tension increment of the electrolyte, the larger the detachment-period value. As shown in Figure 5d, the solute Marangoni effect dominates in the small overpotential region. In conclusion, due to the different surface-tension increments of different electrolytes, the solute Marangoni force acting on individual  $\text{H}_2$  gas bubbles also varies. Additionally, under most practical current density conditions, the operation of  $\text{H}_2$  gas bubbles must consider the solute Marangoni effect.

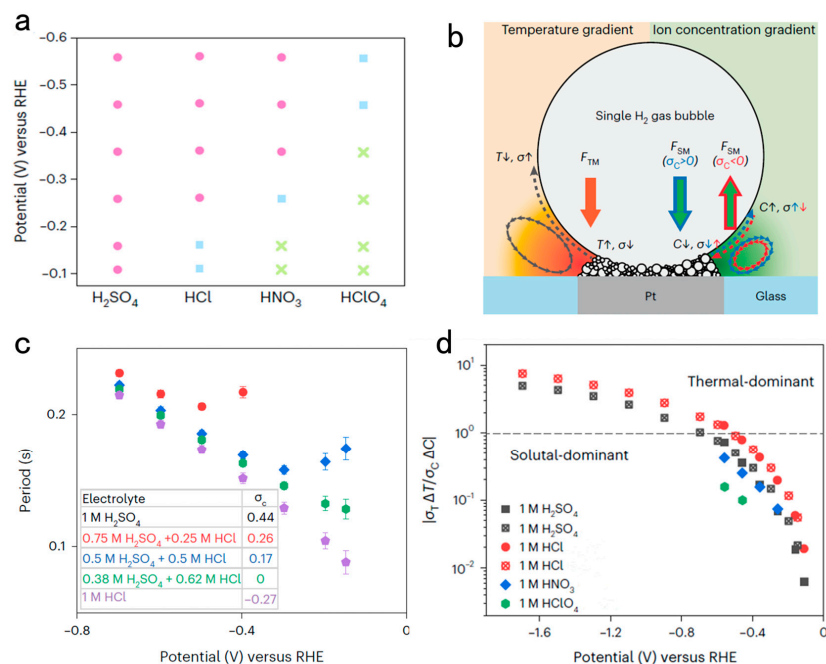


**Figure 5.** (a) Phase diagram of different gas-bubble-evolution patterns at each condition. The pink circles represent periodic disengagement of large hydrogen bubbles. The light green cross represents aperiodic detachment of small hydrogen bubbles. The light blue box represents the middle state between the first two. (b) The thermal and solutal Marangoni effects on  $\text{H}_2$  gas-bubble evolution. (c) Enlarged plot of the dashed grey box. (d) Surface-tension-change ratio due to the temperature and ion concentration. Reproduced with permission from [85], © 2023 Nature Publishing Group.

### 3.2. Effect of Mechanical Vibration and Water Velocity on Bubble Management in PEM Electrolysis Cell

Mechanical vibration can affect bubble detachment by altering the fluid dynamics within the electrolysis cell and the interaction between bubbles and the electrode surface. Water-flow velocity is also a significant factor influencing bubble detachment, as higher flow rates may facilitate easier detachment of bubbles from the electrode surface [86]. Mechanical vibration alters the fluid dynamics within the electrolysis cell, including the flow patterns and velocity distribution. This can impact the adhesion force between bubbles and the electrode surface, thereby affecting bubble detachment. Higher water flow velocities reduce the time bubbles remain attached to the electrode surface, consequently decreasing the adhesion force between bubbles and the electrode surface, making bubble detachment easier [87]. Both mechanical vibration and water-flow velocity can influence the bubble-detachment process, but their specific effects depend on the design parameters of the electrolysis cell, operating conditions, and electrolyte properties.

Di Zhu et al. reported variability in the bubble dynamics and two-phase flow performance of PEMEC at different amplitudes, frequencies, and water-flow rates, and analyzed the correlation between the findings and the electrochemical performance. Firstly, the effect of different amplitudes was observed under operation with a water-flow rate of 10 mL/min and a frequency of 40 Hz. At 0.5 A/cm<sup>2</sup>, an increase in amplitude was associated with an increase in the area ratio of the annular flow, while the area ratio of the bubble flow decreased [88]. With the water-flow rate and frequency fixed, higher amplitude and current density resulted in a higher annular flow-area ratio and smaller bubble formation, which is less likely to produce bubbles (Figure 6a). Additionally, the bubble coverage in the flow channel is depicted in Figure 6b, and the results show that the bubble coverage increases with the increase in amplitude. The bubble coverage in the flow channel increased under vibration conditions compared to no-vibration conditions. This indicates that vertical-sinusoidal vibration can alleviate gas clogging, and the larger the vibration amplitude, the better the relief effect. However, the effect of vibration amplitude on optimizing the electrochemical performance of PEMEC is not infinite. From Figure 6c,d, under constant water-flow rate and amplitude, the area ratio of the annular flow tends to decrease with the increase in frequency, suggesting that the increase in vibration frequency promotes the transformation of annular flow to slug flow and bubble flow. The increase in frequency shortens the cycle time for bubble bursting and gas expulsion, significantly improving performance. However, when the current density is too high, the effect of frequency increase on performance optimization is significantly reduced. Based on constant amplitude and vibration frequency, an increase in current velocity leads to an increase in the proportion of bubble flow. As the bubble volume increases, the shear force generated by the water flow on the bubble increases. When the volume of the bubble reaches a critical value, the bubble is released from its growing position by the sheer force of the water flow. As the velocity of the water flow increases, the thrust force generated by the water flow increases, and the radius of bubble detachment decreases. The increase in water velocity has a significant effect on removing bubbles from the flow path (Figure 6e,f). The electrochemical performance of the electrolyzer was optimized with the increase in amplitude, frequency, and water velocity.

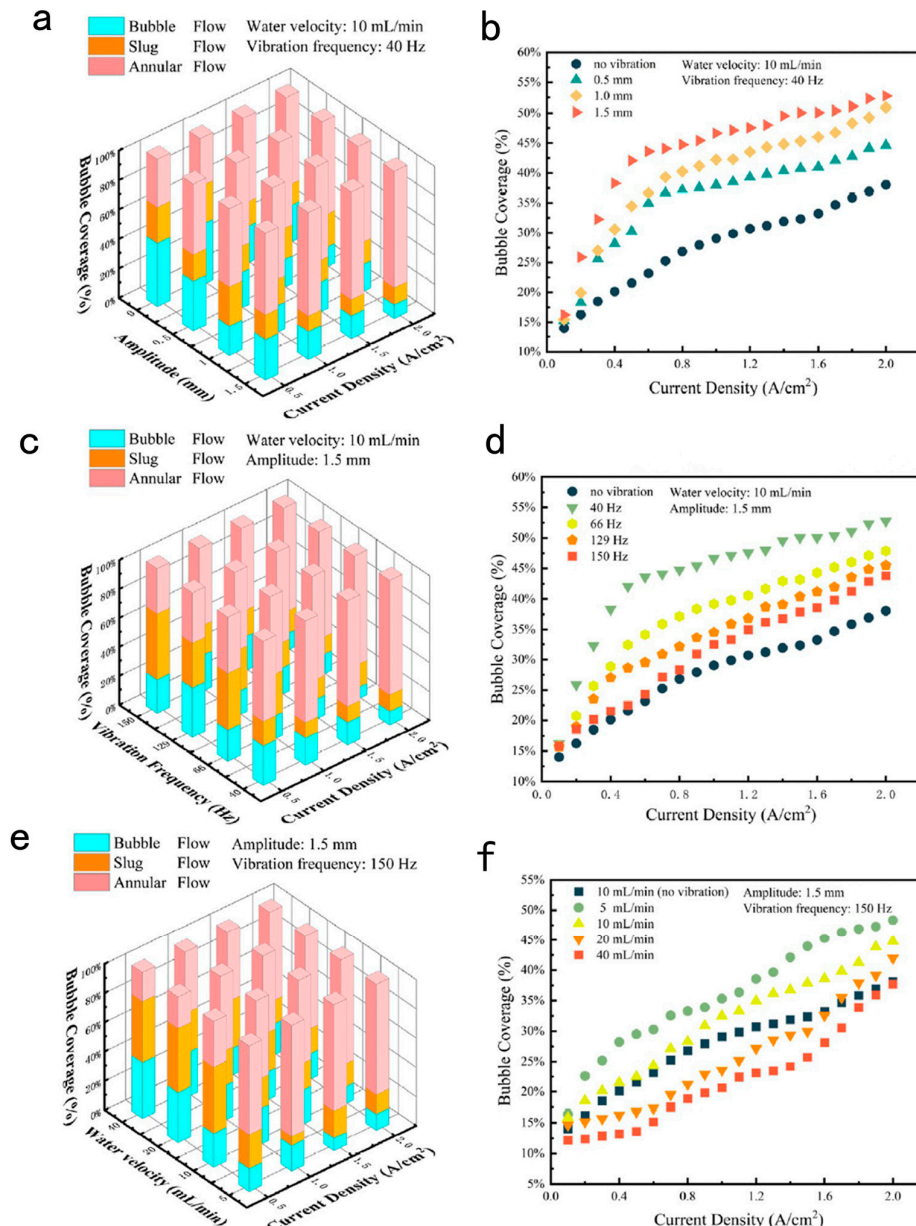


**Figure 6.** (a) Area ratio of flow patterns in different amplitudes. (b) Bubble coverage of proton exchange membrane hydrolysis cell (PEMEC) at different amplitudes. (c) Area ratio of flow patterns in different frequencies. (d) Bubble coverage of PEMEC at different frequencies. (e) Area ratio of flow patterns in different water velocities. (f) Bubble coverage of PEMEC at different water velocities. Reproduced with permission from [88], © 2023 Elsevier.

### 3.3. Effect of Orientation, Rotation, and Sonication on Bubble Management

Orientation force involves applying an external force field to guide the movement of bubbles along specific paths, thereby facilitating bubble detachment from the electrode surface. Rotation alters the fluid flow patterns and distribution of bubbles, making it easier for bubbles to detach from the electrode surface and aiding in their removal from the electrolysis cell [89,90]. Sonication treatment disrupts the adhesion force between bubbles and the electrode surface, promoting bubble detachment [91,92]. Additionally, sonication waves can generate microbubbles and eddies in the liquid, facilitating the expulsion of bubbles from the electrolysis cell. Overall, orientational, rotational, and sonicated treatments affect bubble detachment by altering the interaction between bubbles and the electrode surface. These methods enhance the efficiency of bubble detachment

in water-electrolysis processes, leading to improved electrolysis efficiency and hydrogen production rates.

Workers have conducted new research on bubble-removal strategies from the perspectives of catalyst quality and activity, catalyst loss, charge transfer, and reaction overpotential. As the WE direction increases, the mass loss of Ir increases. Changing the WE orientation has a significant impact on OER activity [93]. In addition, the OER activity and Ir loss mechanism of the catalyst can be corrected through rotational speed. As shown in Figure 7a, the bubbles can easily slide on the catalyst surface and merge with other corresponding bubbles. The use of rotating disc electrodes (RDE) not only improved the OER performance of the catalyst but also reduced the overpotential compared to W0. Significant Ir loss may be related to Ir detachment from the surface due to severe rotation. The ultrasonic field significantly improves the OER activity of the electrode, the erosion caused by acoustic cavitation leads to physical detachment of the catalyst layer. As shown in Figure 7b, higher ultrasonic power can more effectively remove surface bubbles, thereby enhancing the quality activity of samples treated with high-power ultrasound. The highest OER activity and suitable charge transfer mechanism are shown. This improvement is maximized when both RDE and ultrasound are used simultaneously. The introduction of ultrasonic fields completely changed the charge transfer mechanism. The shielding effect originates from a thin unstirred layer near the surface of the catalyst, outside which convection cannot accelerate the transfer of mass and charge. This static behavior of the electrolyte leads to the accumulation of bubbles within the Nernst diffusion layer (NDL) layer, trapping them in the porous structure of the catalyst. The increase in the characteristic frequency and the decrease in impedance result in a high rate of charge transfer through the electrical bilayer. In summary, changing the orientation of WE promotes the aggregation and sliding of bubbles, while the rotational convection of WE significantly improves the mass-transfer mechanism. In addition, the application of ultrasonic fields can minimize the screening effect of double layers formed near the catalyst layer.

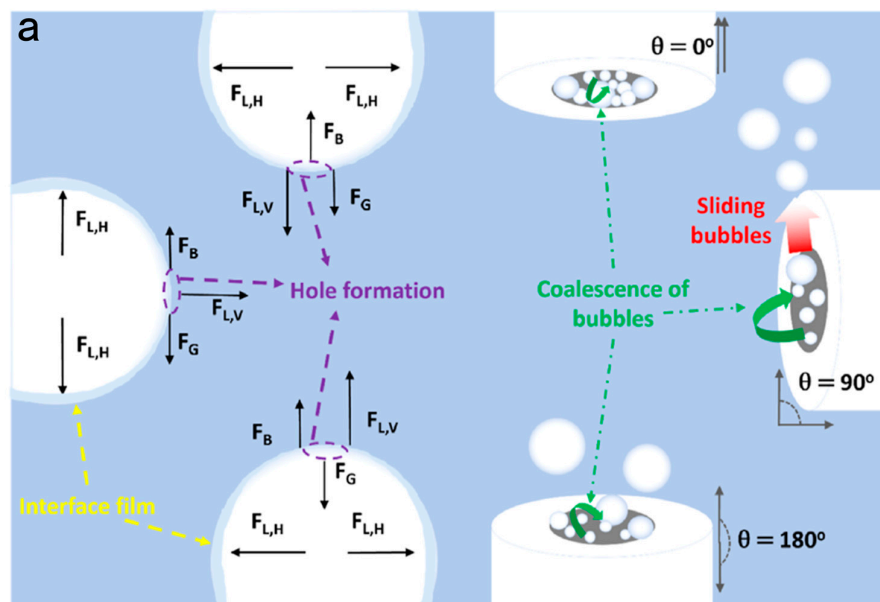


**Figure 7. Cont.**

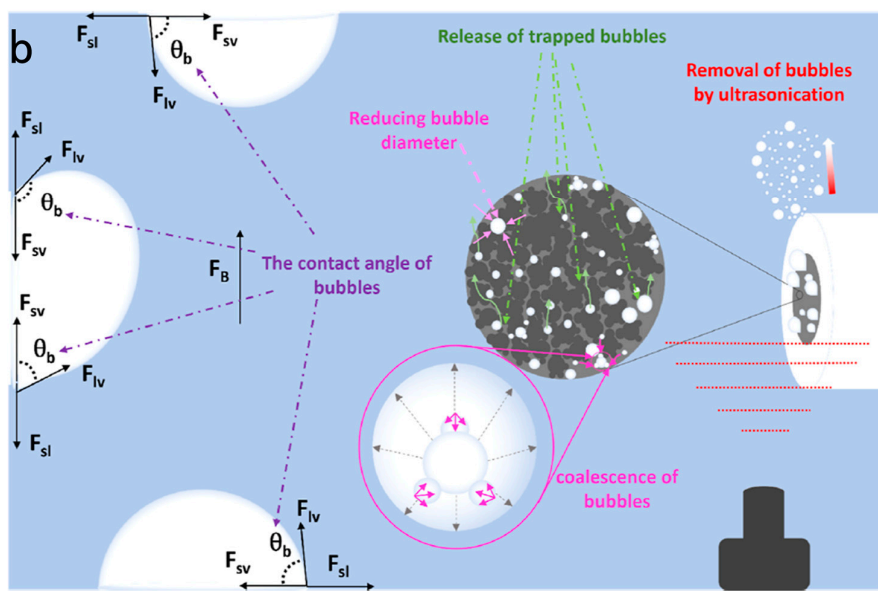


**Figure 7.** (a) Effects of coalescence and sliding of bubbles in bubble collapse and improving the OER performance for different orientations of the working electrode (WE). The green arrows represent coalescence. The red arrows represent bubbles sliding. The purple arrow represents the formation of the hole. The yellow arrow indicates the thinnest part of the interface film. (b) Schematic of bubble removal using an ultrasonication field by two major effects. The red text refers to the physical power generated by the ultrasonic field. The pink text refers to the coalescence of bubbles. The green text refers to the release of small bubbles. The purple text refers to the contact Angle of the catalyst surface. Reproduced with permission from [93], © 2023 American Chemical Society.

#### 4. Design of Catalysts to Promote Bubble Detachment

There are several catalyst-design strategies aimed at promoting bubble separation. For instance, fine-tuning the catalyst composition can significantly improve its efficacy. This involves adjusting the ratio of active metals, carriers, and promoters to maximize catalytic activity, selectivity, and stability [94]. Furthermore, modifying the catalyst structure at the nano or micro scale can be instrumental in improving performance. This may entail controlling particle size, morphology, surface area, and pore-size distribution to optimize catalytic activity and enhance the accessibility of active sites [95]. Additionally, introducing functional groups or modifiers on the catalyst surface can augment the interaction between the catalyst and reactants, facilitating the adsorption/desorption process, and thereby improving catalytic selectivity and stability [96]. Moreover, the selection of a suitable support material holds great influence over catalyst performance. Adjusting the surface chemistry, porosity, and mechanical properties of the support can enhance the dispersion, stability, and mass transfer performance of the active components. Continuously exploring and discovering novel catalytic materials, including metal-organic frameworks (MOFs), covalent organic frameworks (COFs), and hybrid materials, can open up new opportunities for improving catalytic performance [97]. Enhancing surface hydrophobicity, controlling microstructure, optimizing active sites, and modifying surface properties are commonly employed strategies. Designing electrode surfaces with high hydrophobicity can reduce bubble attachment and accelerate their rapid detachment. This can be achieved through surface coatings or manipulating the electrode surface structure, including the introduction of hydrophobic functional groups or the fabrication of micro/nanostructured surfaces. Microstructural designs, such as nanopores, micropores, or hierarchical pore structures, optimize bubble-surface interactions by modulating the morphology, structure, and energetic properties of the electrode surfaces, thereby increasing the efficiency of bubble detachment and, consequently, the efficiency and stability of the water-electrolysis process. Optimizing the active sites of a catalyst directly affects aspects of its surface composition,

structure, density, and electronic structure, which in turn changes its surface energetic and chemical properties. These changes can significantly impact the catalytic performance and reactivity of the catalyst, enabling precise control and optimization of the catalytic reaction. Modulating the surface-energy distribution on the electrode surface can reduce the ability of bubbles to adhere to the surface. By reducing the surface energy of the area, the interaction force between bubbles and the surface can be minimized, thus decreasing the residence time of bubbles on the surface, and promoting their rapid detachment. In conclusion, by comprehensively considering surface properties, microstructure, active sites, and external field effects, efficient catalysts with good bubble detachment performance can be designed to improve the efficiency and stability of water electrolysis.

#### 4.1. Design of Nanoarrays toward Efficient Electrochemical Water Splitting

The design of nano-arrays plays a crucial role in facilitating bubble separation through a variety of strategies, including increasing surface area, decreasing surface tension, improving hydrodynamics, and enhancing catalytic activity [98–100]. Together, these strategies help reduce the adhesion of gas bubbles to the electrode during electrolysis, thereby promoting rapid bubble separation and improving the efficiency and stability of the water-splitting reaction [101,102]. Firstly, the nanostructured surface with more microscopic voids and irregular morphology can reduce the contact area between water molecules and the electrode surface, thus reducing the adhesion of gas bubbles to the electrode surface and promoting bubble detachment [103]. Secondly, the microstructure of the nanoarrays can change the flow pattern of the electrolyte solution, such as increasing turbulence or changing the flow rate distribution, thus affecting the movement and detachment of bubbles [104–106]. Finally, the high specific surface area and abundant active sites of the nanoarrays are expected to improve the catalytic activity of the electrochemical reaction, thereby promoting bubble detachment, and facilitating the water-splitting reaction [107,108].

The three-phase contact line (TPCL) affects the attachment and detachment of bubbles to the electrode surface. Inside the TPCL, the bubbles are in direct contact with the electrode surface and the adhesion force is greater, so the bubbles are more likely to attach to the electrode surface. Outside the TPCL, the presence of the liquid medium reduced the contact between the bubbles and the electrode surface, making it easier for the bubbles to detach from the surface. Therefore, modulating the position and characteristics of the TPCL can influence the attachment and detachment process of the bubbles. Nanoarrays exhibit superhydrophobicity and superhydrophilicity properties, which can repel bubbles and further facilitate their effective detachment. Huang et al. utilized phase-field simulations to evaluate the influence of dynamic electrolyte flow on bubble detachment from surface array electrodes. Under static conditions, as shown in Figure 8a, bubbles detach when buoyancy exceeds adhesion forces, and shear forces generated by the electrolyte flow also contribute to bubble detachment [109]. As shown in Figure 8b, as the surface roughness increases, the contact angle between bubbles and solid surfaces significantly increases, exhibiting superhydrophobicity and significantly reducing contact area and adhesion, thereby promoting bubble separation, and reducing bubble size during separation. The interaction between buoyancy and adhesion between the bubble and the substrate affects the desorption of the bubble [110]. The depth of bubbles and conical decorative surfaces is shown in Figure 8c, the interlayers in LFA provide continuous and ordered microchannels for bubble transport, showing a dynamically adaptive characteristic upon bubbling. The mirror-symmetrical and parallelly layered fern-like structures in the LFA electrode facilitate bubbles releasing along the direction of buoyancy throughout the interlayers [111]. This process of facet engineering, transforming NF into nickel foam with mountain-shaped nanostripes (NFMN), is schematically represented by the pink arrow route in Figure 8d [112]. The best strategy for the enhanced HER activity of the super-hydrophobic Ni-80 catalyst is shown in Figure 8e [113]. In conclusion, employing micro- and nanostructures to adjust the morphology and roughness of the catalyst surface, as well as transforming it into a more hydrophobic feature, can increase the water contact angle of the surface. Consequently, this

reduces the adhesion of gas bubbles on the surface, facilitating rapid bubble separation and enhancing the efficiency and stability of the water-decomposition reaction. In summary, nanoarray design is of great significance for achieving efficient water decomposition and can provide guidance for catalyst design. Nanoarrays can provide a large amount of active surface area, allowing the water-decomposition catalyst to adsorb water molecules more efficiently and perform the reaction [114]. In addition, the nanoarray design can precisely control the distribution and structure of the active site of the catalyst, so as to achieve the regulation of reaction activity and selectivity. The density and distribution of catalytic active sites can be optimized and the activity and stability of catalysts can be improved by rational design of nanostructures [115].

#### 4.2. Enhancing Catalyst-Carrier Interface Binding

By designing electrocatalysts with hydrophobic surfaces or micro/nanostructures, the adhesion force of bubbles to the surface can be reduced, thereby facilitating the rapid detachment of bubbles [116]. This helps decrease the time bubbles remain on the electrode surface, thus improving the efficiency of the electrolysis process. Introducing strong binding forces at the catalyst-carrier interface enhances the stability and durability of the catalyst [117]. While this may increase the adhesion force of bubbles to the carrier surface, optimizing the interface structure can minimize hindrance to the catalyst's active sites, ensuring long-term stable operation. Combining the strategies of weak bubble adhesion and strong catalyst-carrier interface binding allows for effective control of the bubble detachment process, enhancing bubble separation efficiency, reducing interference from bubbles in the electrolysis process, and thereby improving the efficiency and stability of the water splitting reaction.

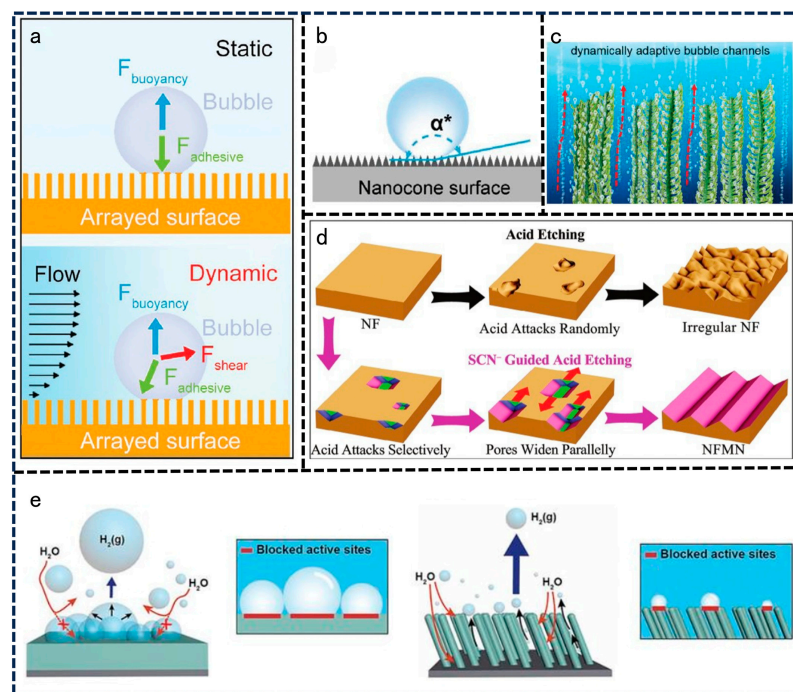


**Figure 8.** (a) Force analysis of a gas bubble on surface-arrayed electrode under static and dynamic conditions. Reproduced with permission from [109], © 2023 Wiley-VCH. (b) Schematic illustration of bubble-contact angle, area, and evolution on an NC-modified Ni surface.  $\alpha^*$  indicates the apparent bubble contact Angle between the rough surface and the liquid. Reproduced with permission from [110], © 2023 Wiley-VCH. (c) Schematic illustration of the bubble-transport behavior for  $O_2$  bubbles in the lamellar fern-like alloy aerogel (LFA). Reproduced with permission from [111], © 2023 Wiley-VCH. (d) Schematic illustration for SCN<sup>-</sup>guided acid etching of NF. Reproduced with permission from [112], © 2023 Wiley-VCH. (e) Schematic illustration of the  $H_2$  bubble-release behavior of the Ni film and the Ni-80 catalysts. Reproduced with permission from [113], © 2023 Wiley-VCH.

At high current densities, the detachment of many bubbles creates a strong electrocatalyst-bubble adhesion force. When it is greater than the bonding force between the electrocatalyst and the support, it causes the electrocatalyst to detach. Therefore, it is important to improve the mechanical stability of the electrode by enhancing the adhesion force between the electrocatalyst and the support and weakening the interfacial force between the electrocatalyst and the bubbles [118]. Heming Liu et al. reported a mechanically stable, all-metal, highly active CuMo<sub>6</sub>S<sub>8</sub>/Cu electrode constructed through an in situ reaction between MoS<sub>2</sub> and copper. As depicted in Figure 9a, during the annealing process, copper atoms react with MoS<sub>2</sub>, undergoing an in situ transformation to form the Chevrel phase CuMo<sub>6</sub>S<sub>8</sub>. This transformation effectively eliminates Schottky barriers formed prior to annealing and enhances electron transfer from the support to the electrocatalyst. Figure 9b illustrates the variation in the onset potential of the CuMo<sub>6</sub>S<sub>8</sub>/Cu electrode. This difference arises from the stripping process of the electrocatalyst, where a larger difference indicates more pronounced stripping. The region with small differences below 0.05 V predominantly encompasses the CuMo<sub>6</sub>S<sub>8</sub> electrode. This finding suggests that CuMo<sub>6</sub>S<sub>8</sub>/Cu electrodes exhibit strong mechanical stability and form a robust interfacial bond through chemical covalent bonding compared to conventional adhesives. As shown in Figure 9c, CuMo<sub>6</sub>S<sub>8</sub> detaches from the support at a load of 1.15 N, whereas Pt/C detaches at a load of 0.58 N. The CuMo<sub>6</sub>S<sub>8</sub>/Cu electrodes also exhibit greater stability than conventional electrodes. The enhanced interfacial bonding and reduced interfacial adhesion of the electrocatalyst bubbles contribute to the mechanical stability and performance of CuMo<sub>6</sub>S<sub>8</sub>/Cu electrodes at high current densities. Figure 9d shows that the initial potentials of Pt/C and CuMo<sub>6</sub>S<sub>8</sub>/Cu electrodes are  $-86$  mV and  $-165$  mV, respectively, relative to the reversible hydrogen electrode (RHE), confirming the reliability of the TIR imaging method. Figure 9e displays the active sites for HER on the three main crystallographic planes of CuMo<sub>6</sub>S<sub>8</sub> and their corresponding free-energy diagrams. The adsorption of free energy of H<sup>\*</sup> ( $\Delta G_{H^*}$ ) serves as a rational description of HER activity. An ideal HER electrocatalyst should have a moderate  $\Delta G_{H^*}$  close to 0 eV. To sum up, CuMo<sub>6</sub>S<sub>8</sub>/Cu features a strong electrocatalyst-support binding force and a weak electrocatalyst-bubble adhesion force. The homologous metal double interface electrode can effectively utilize the high electrical conductivity and catalytic activity of the metal to improve the rate and efficiency of the water decomposition reaction [119]. In addition, the homologous metal double interface electrode design can not only optimize the electron transport path but also improve the electron transport rate on the electrode surface [120]. It can also enhance the catalytic activity at the interface and promote the adsorption and decomposition of water molecules on the electrode surface [121]. The catalytic activity and selectivity of the catalyst for the water-decomposition reaction can be enhanced by designing the interface structure and the distribution of surface-active sites reasonably.

#### 4.3. Bioinspired Trimesic Acid Anchored Electrocatalysts

The superhydrophobic surface facilitates the timely release of generated oxygen bubbles and protects the structure of the catalyst. The covalent bond coupling between the metal and the coordinating carboxylate prevents the dissolution of the metal species, thus stabilizing the electronic structure through static coordination [122]. Additionally, the unliganded carboxylates formed through dynamic evolution can act as proton ferries to accelerate the kinetics of the oxygen-evolution reaction. Unliganded carboxylates can facilitate the desorption of gas bubbles by modulating surface energy and interfacial activity. When gas bubbles encounter surfaces modified with unliganded carboxylates, their surface tension decreases, making it easier for the bubbles to desorb from the surface. This phenomenon increases the solubility of the gas in the liquid, thereby facilitating the release of the bubbles. Moreover, non-coordinating carboxylates can form an adsorbent layer at the interface, which reduces the nucleation and growth of gas bubbles, thus facilitating the desorption process of gas bubbles [123]. Thus, non-coordinating carboxylates play a role in bubble desorption by modulating surface properties and reducing interfacial energy, thereby facilitating the release of bubbles.

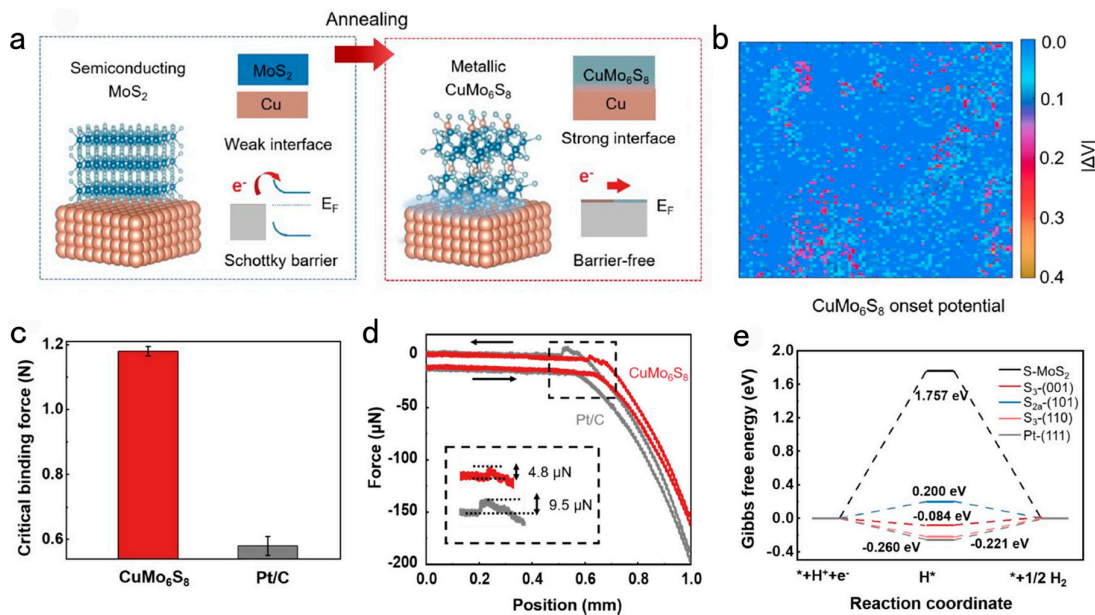


**Figure 9.** (a) A schematic showing the preparation process e of CuMo<sub>6</sub>S<sub>8</sub>/Cu electrode. (b) The relationships between incident angle, equivalent refractive index, and reflectivity. (c) The statistical data of critical adhesive forces of CuMo<sub>6</sub>S<sub>8</sub> and Pt/C. (d) The relationships between the onset potential of the electrode and light intensity. (e) Gibbs free energy ( $\Delta G^\circ$ ) variations for HER on best active sites of three facets of CuMo<sub>6</sub>S<sub>8</sub>, sulfur site of MoS<sub>2</sub> and Pt (111). \* represents adsorption free energy. Reproduced with permission from [118], ©2022 Nature Publishing Group.

NiFe-LDH exhibits excellent performance in the OER due to its unique two-dimensional lamellar structure and controllable electronic properties. Difficulty in breaking the kinetic bottleneck remains a key factor limiting the activity at high current densities. Therefore, an in-depth understanding of the active site and structural features of LDH is necessary to tailor improved kinetics and stability. Xiaojing Lin et al. reported a sub-sized NiFe-LDH nanosheet catalyst modified with tris hydroxymethyl carbamate acid (SU-NiFe-LDH(TA)). Figure 10a–c shows the contact angle test results for NiFe-LDH@cp, NiFe-LDH(TA)@cp, and SU-NiFe-LDH(TA)@cp. The contact angles of ultrapure water on NiFe-LDH@cp and nfe-ldh(TA)@cp were 18° and 15°, respectively, while the contact angle on su-nfe-ldh(TA)@cp was close to 0°. The smaller nanoplatelet surfaces of su-nfe-ldh(TA)@cp were much rougher and exhibited superhydrophilicity. These apparent changes suggest that the insertion layer formed by cyanuric acid increases the rate of electrolyte diffusion on the surface and between the layers [124]. In addition, the cavitation effect due to bubble rupture can severely damage the nanostructures, and the evolution of bubbles on the electrode surface affects the stability of the structure [125]. Figure 10d–f show the formation and release of oxygen bubbles in 40 s. The bubble adheres firmly to the NiFe-LDH@cp electrode surface and grows into a large 34.67  $\mu\text{m}$  bubble. In contrast, the oxygen bubble is much smaller before escaping from LFE-LDH(TA)@cp and SU-NiFe-LDH(TA)@cp. In particular, the diameter of the oxygen bubble on SU-NiFe-LDH(TA)@cp is smaller. This means that the oxygen bubbles break away immediately after formation, allowing the catalytic site to be re-exposed to the surrounding electrolyte more quickly. The superhydrophobicity and superhydrophilicity of Su-NF<sub>el</sub>-LDH (TA) @cp accelerate the release and mass transfer of bubbles, thereby improving the activity and stability. The design of the bioinspired trimesic acid anchored catalyst takes into account the selection and fixation of the active group, which can improve catalytic activity and stability. Additionally, the design of the bioinspired trimesic acid anchored catalyst mimics the optimized electron transport pathway found in biocatalysts, thereby increasing the efficiency and rate of the water-decomposition reaction [126]. Bio-heuristically designed catalysts are generally renewable and environmentally friendly, helping to reduce energy consumption and environmental impact [127].

In summary, by simulating the catalytic mechanism in organisms, improving catalytic activity and stability, optimizing electron-transport pathways, and reducing energy consumption and environmental impact, the goal of efficient water decomposition can be achieved, and the development and application of related technologies can be promoted.

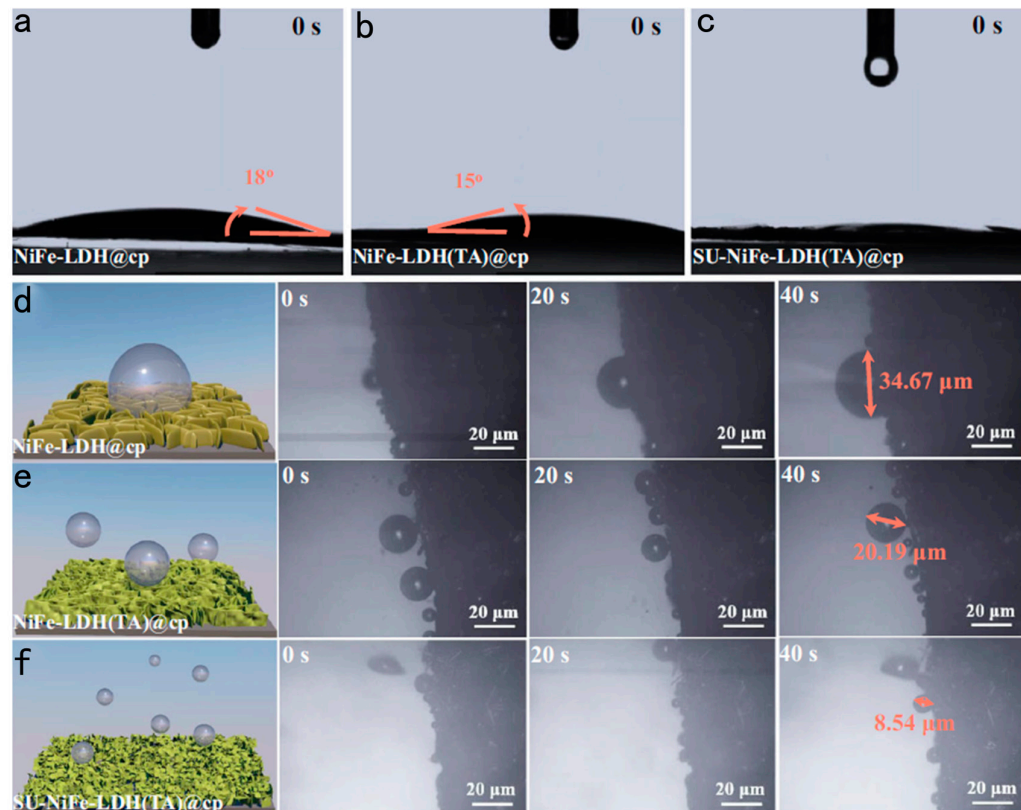


**Figure 10.** Production and detection of in situ adhesion behavior. (a–c) The contact angle of ultrapure water on NiFe-LDH@cp, NiFe-LDH(TA)@cp, and SU-NiFe-LDH(TA)@cp. (d–f) In situ detection of precipitation behavior of  $O_2$  on NiFe LDH@cp, NiFe-LDH(TA)@cp, and SU-NiFe-LDH(TA)@cp at  $10\text{ mAc}\text{m}^{-2}$ , respectively. Reproduced with permission from [124], © 2023 Nature Publishing Group.

#### 4.4. Design of 3D Nano Graded Catalyst Materials

A three-dimensional (3D) crisscross mesoporous design with layered isolation enables bubbles to move freely along interconnected channels, reducing obstruction and increasing the overall transport rate, thereby enhancing diffusion efficiency. Additionally, 3D nanostructures can alter the flow pattern of the electrolyte solution by increasing turbulence or modifying the flow-rate distribution, thereby influencing the movement and detachment of bubbles [128,129]. In conclusion, the utilization of 3D nanostructures can significantly improve bubble-separation efficiency and optimize the water-electrolysis reaction.

Zhenhui Liu et al. have proposed a nanoscale hierarchical strategy to address this issue, employing catalyst carbon supports with 3D interwoven mesopores to facilitate limited mass transport, thereby allowing hydrogen bubbles to diffuse effectively along interconnected pathways [130]. As illustrated in Figure 11a, electrode structures such as catalyst coating membranes, fiber catalyst layers, nanoarrays, and microporous frameworks with ultra-nonwetting surfaces and excellent electrolyte wettability are designed to minimize bubble growth and accelerate separation. However, mass transport cannot be adjusted at the nanoscale. Workers have utilized ordered 3D interconnected sub-5 nm pores to achieve sub-nanometer-constrained mass transport. As shown in Figure 11b, utilizing atomic electron tomography, researchers can observe the rich and ordered mesopore distribution on individual particles of Ru/3d-OMC. This confirms the presence of continuous interconnected mesoporous channels in Ru/3d-OMC. As shown in Figure 11c, the  $H_2$  con-

centration in Ru/2d-OMC is consistently higher than that in Ru/3d-OMC, suggesting that more H<sub>2</sub> molecules are blocked in the non-interconnected parallel mesoporous channels of Ru/2d-OMC. The bubbles in the 3D mesoporous channels were able to detach quickly. As shown in Figure 11d, the outlet flux of Ru/3d-OMC is nearly ten times that of Ru/2d-OMC, demonstrating the capability of Ru/3d-OMC to simultaneously transport more H<sub>2</sub>. In summary, 3D interconnected mesopores offer significant advantages. Introducing appropriately sized and designed micropores to connect mesoporous channels would further enhance the efficiency of H<sub>2</sub> transport. Through the nanoscale fractionation-separation strategy, the catalyst structure can be optimized, increasing its surface area and exposure of active sites. This not only enhances the catalyst's interaction with water molecules but also promotes the water-decomposition reaction [131]. Moreover, it optimizes the path of electron transport within the catalyst and improves the electron transmission rate on its surface. Catalyst strategies such as changing the surface structure, designing catalysts with good structural characteristics, and heteroatom doping can effectively reduce bubble side effects and improve water splitting efficiency. Table 1 lists the performance data of different catalysts using surface structure modification in recent years.

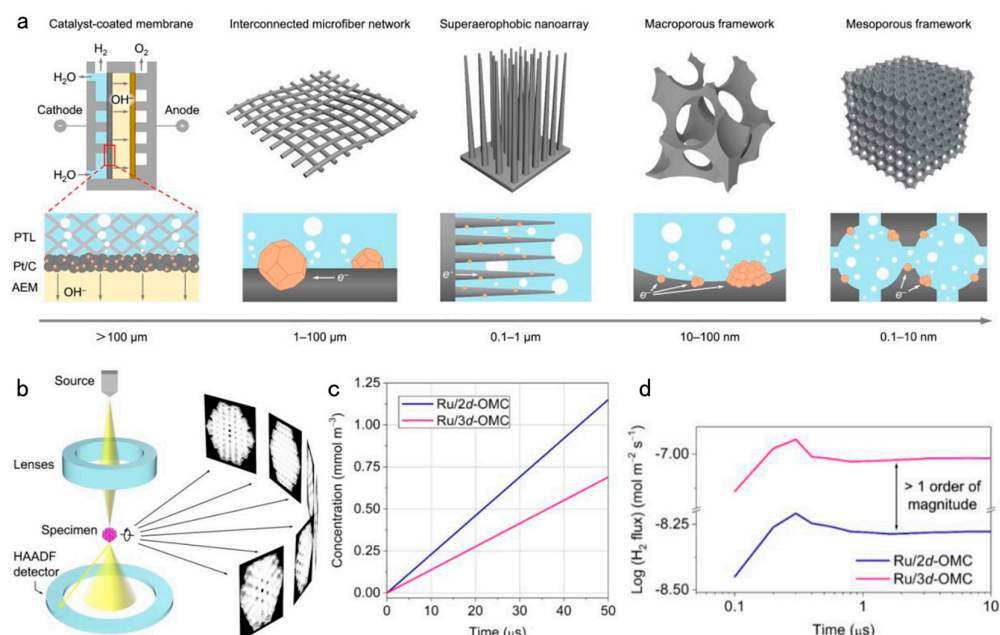


**Figure 11.** (a) Schematic diagrams of H<sub>2</sub> gas diffusion on catalyst-electrolyte interface for different types of electrode structures. (b) Schematic diagram of electron microscope tomography. (c) H<sub>2</sub> concentration-time curves. (d) Total flux of H<sub>2</sub> as a function of time. Reproduced with permission from [130], © 2023 Wiley-VCH.

**Table 1.** Comparison of HER performance on different catalysts.

Catalyst	$\eta@10 \text{ mA cm}^{-2}$ (mV)	$\eta@100 \text{ mA cm}^{-2}$ (mV)	$\eta@500 \text{ mA cm}^{-2}$ (mV)	$\eta@1000 \text{ mA cm}^{-2}$ (mV)	Tafel Slope (mV dec <sup>-1</sup> )	Ref.
sFNSNA	191	255	-	-	-	[109]
LFA	192	-	238	242	29.2	[111]
NFMN-FeOOH	-	-	308	-	36	[112]
Ni-80	135	271	-	-	-	[113]
CuMo <sub>6</sub> S <sub>8</sub> /Cu	-	-	-	-	32.5	[118]
SU-NiFe-LDH(TA)	219	-	-	-	31.1	[124]
Ru/3d-OMC	20	-	-	-	46.68	[130]

## 5. Conclusions and Outlooks

In the field of water electrolysis, a thorough investigation into the bubble-detachment process is crucial for enhancing electrolytic efficiency and hydrogen gas yield. Utilizing advanced characterization techniques such as high-frequency impedance spectroscopy, atomic force microscopy, and chronoamperometry, we can monitor the dynamic evolution of bubbles in real-time and non-invasively, providing detailed insights into bubble-detachment behavior. The factors influencing bubble detachment are multifaceted, including fluid dynamics within the electrolyzer, electrolyte properties, and current density. Surface characteristics, electrolyte concentration, bubble size and morphology, and flow conditions all play significant roles in bubble detachment. The interaction between these factors requires further investigation to comprehensively understand the mechanism of bubble detachment. In terms of catalyst design, introducing weak adhesion at the bubble interface and strong bonding at the catalyst-carrier interface is an effective strategy. Designing electrocatalysts with hydrophobic surfaces or nanostructured features can reduce bubble adhesion, thereby facilitating rapid bubble detachment. Meanwhile, introducing strong bonding at the catalyst-carrier interface can enhance the stability and durability of the catalyst, ensuring long-term efficient operation.

Future work should focus on further innovation and improvement of characterization techniques to obtain more precise information about bubble detachment. Moreover, there is a need for in-depth studies on the mechanism of bubble detachment, especially under different process conditions. In catalyst design, a multidisciplinary approach integrating surface properties, microstructure, active sites, and external field effects should be pursued to achieve more effective control over the bubble-detachment process. Through continuous efforts and deep research, we can expect to better understand and control the mechanism of bubble detachment, driving the development of water-electrolysis technology and providing more efficient solutions for sustainable clean energy production.

**Author Contributions:** Writing—review and editing, Z.Z., C.G., K.W., H.Y., J.Q. and S.W.; project administration, L.W. and D.Y. All authors have read and agreed to the published version of the manuscript.

**Funding:** This work was financially supported by the Natural Science Foundation of China (22202065).

**Data Availability Statement:** Data are contained within the article.

**Conflicts of Interest:** The authors declare that they have no known competing financial interests or personal relationships that could have appeared to influence the work reported in this paper.

## References

1. Zhao, X.; Ren, H.; Luo, L. Gas Bubbles in Electrochemical Gas Evolution Reactions. *Langmuir* **2019**, *35*, 5392–5408. [[CrossRef](#)] [[PubMed](#)]
2. Leal Pérez, B.J.; Medrano Jiménez, J.A.; Bhardwaj, R.; Goetheer, E.; van Sint Annaland, M.; Gallucci, F. Methane pyrolysis in a molten gallium bubble column reactor for sustainable hydrogen production: Proof of concept & techno-economic assessment. *Int. J. Hydrogen Energy* **2021**, *46*, 4917–4935. [[CrossRef](#)]
3. Ketzer, M.; Praeg, D.; Rodrigues, L.F.; Augustin, A.; Pivel, M.A.G.; Rahmati-Abkenar, M.; Miller, D.J.; Viana, A.R.; Cupertino, J.A. Gas hydrate dissociation linked to contemporary ocean warming in the southern hemisphere. *Nat. Commun.* **2020**, *11*, 3788. [[CrossRef](#)] [[PubMed](#)]
4. Rest, J.; Cooper, M.W.D.; Spino, J.; Turnbull, J.A.; Van Uffelen, P.; Walker, C.T. Fission gas release from UO<sub>2</sub> nuclear fuel: A review. *J. Nucl. Mater.* **2019**, *513*, 310–345. [[CrossRef](#)]
5. Frinking, P.; Segers, T.; Luan, Y.; Tranquart, F. Three Decades of Ultrasound Contrast Agents: A Review of the Past, Present and Future Improvements. *Ultrasound Med. Biol.* **2020**, *46*, 892–908. [[CrossRef](#)]
6. Xu, H.; Li, S.; Zhang, C.; Chen, X.; Liu, W.; Zheng, Y.; Xie, Y.; Huang, Y.; Li, J. Roll-to-roll prelithiation of Sn foil anode suppresses gassing and enables stable full-cell cycling of lithium ion batteries. *Energy Environ. Sci.* **2019**, *12*, 2991–3000. [[CrossRef](#)]
7. Shen, J.; Zheng, Y.; Lei, W.; Shao, H. Unraveling the Fundamental Concepts of Superaerophobic/Superhydrophilic Electrocatalysts for Highly Efficient Water Electrolysis: Implications for Future Research. *ChemElectroChem* **2023**, *11*, e202300465. [[CrossRef](#)]
8. Walter, M.G.; Warren, E.L.; McKone, J.R.; Boettcher, S.W.; Mi, Q.; Santori, E.A.; Lewis, N.S. Solar water splitting cells. *Chem. Rev.* **2010**, *110*, 6446–6473. [[CrossRef](#)] [[PubMed](#)]

9. Yan, D.; Mebrahtu, C.; Wang, S.; Palkovits, R. Innovative Electrochemical Strategies for Hydrogen Production: From Electricity Input to Electricity Output. *Angew. Chem. Int. Ed. Engl.* **2023**, *62*, e202214333. [[CrossRef](#)]
10. Cho, H.J.; Wang, E.N. Bubble nucleation, growth, and departure: A new, dynamic understanding. *Int. J. Heat Mass Transf.* **2019**, *145*, 118803. [[CrossRef](#)]
11. Li, Y.; Zhou, W.; Zhang, Y.; Qi, B.; Wei, J. A molecular dynamics study of surface wettability effects on heterogeneous bubble nucleation. *Int. Commun. Heat Mass Transf.* **2020**, *119*, 104991. [[CrossRef](#)]
12. Pereiro, I.; Fomitcheva Khartchenko, A.; Petrini, L.; Kaigala, G.V. Nip the bubble in the bud: A guide to avoid gas nucleation in microfluidics. *Lab Chip* **2019**, *19*, 2296–2314. [[CrossRef](#)]
13. Zhou, T.-T.; He, A.-M.; Wang, P. Dynamic evolution of He bubble and its effects on void nucleation-growth and thermomechanical properties in the spallation of aluminum. *J. Nucl. Mater.* **2020**, *542*, 152496. [[CrossRef](#)]
14. Sarker, D.; Ding, W.; Hampel, U. Bubble growth during subcooled nucleate boiling on a vertical heater: A mechanistic attempt to evaluate the role of surface characteristics on microlayer evaporation. *Appl. Therm. Eng.* **2019**, *153*, 565–574. [[CrossRef](#)]
15. Chen, Y.-J.; Yu, B.; Zou, Y.; Chen, B.-N.; Tao, W.-Q. Molecular dynamics studies of bubble nucleation on a grooved substrate. *Int. J. Heat Mass Transf.* **2020**, *158*, 119850. [[CrossRef](#)]
16. Ren, T.; Zhu, Z.; Yan, M.; Shi, J.; Yan, C. Experimental study on bubble nucleation and departure for subcooled flow boiling in a narrow rectangular channel. *Int. J. Heat Mass Transf.* **2019**, *144*, 118670. [[CrossRef](#)]
17. Li, M.; Xie, P.; Yu, L.; Luo, L.; Sun, X. Bubble Engineering on Micro-/Nanostructured Electrodes for Water Splitting. *ACS Nano* **2023**, *17*, 23299–23316. [[CrossRef](#)]
18. Shih, A.J.; Monteiro, M.C.O.; Dattila, F.; Pavesi, D.; Philips, M.; da Silva, A.H.M.; Vos, R.E.; Ojha, K.; Park, S.; van der Heijden, O.; et al. Water electrolysis. *Nat. Rev. Methods Primers* **2022**, *2*, 84. [[CrossRef](#)]
19. Xu, W.; Lu, Z.; Sun, X.; Jiang, L.; Duan, X. Superwetting Electrodes for Gas-Involving Electrocatalysis. *Acc. Chem. Res.* **2018**, *51*, 1590–1598. [[CrossRef](#)] [[PubMed](#)]
20. Yang, Q.; Han, Y.; Jia, C.; Wu, J.; Dong, S.; Wu, C. Impeding effect of bubbles on metal transfer in underwater wet FCAW. *J. Manuf. Process.* **2019**, *45*, 682–689. [[CrossRef](#)]
21. Zhang, J.; Dong, F.; Wang, C.; Wang, J.; Jiang, L.; Yu, C. Integrated Bundle Electrode with Wettability-Gradient Copper Cones Inducing Continuous Generation, Directional Transport, and Efficient Collection of H<sub>2</sub> Bubbles. *ACS Appl. Mater. Interfaces* **2021**, *13*, 32435–32441. [[CrossRef](#)] [[PubMed](#)]
22. Angulo, A.; van der Linde, P.; Gardeniers, H.; Modestino, M.; Fernández Rivas, D. Influence of Bubbles on the Energy Conversion Efficiency of Electrochemical Reactors. *Joule* **2020**, *4*, 555–579. [[CrossRef](#)]
23. Darband, G.B.; Aliofkhazraei, M.; Shanmugam, S. Recent advances in methods and technologies for enhancing bubble detachment during electrochemical water splitting. *Renew. Sustain. Energy Rev.* **2019**, *114*, 109300. [[CrossRef](#)]
24. Kim, B.K.; Kim, M.J.; Kim, J.J. Impact of Surface Hydrophilicity on Electrochemical Water Splitting. *ACS Appl. Mater. Interfaces* **2021**, *13*, 11940–11947. [[CrossRef](#)] [[PubMed](#)]
25. Long, Z.; Zhao, Y.; Zhang, C.; Zhang, Y.; Yu, C.; Wu, Y.; Ma, J.; Cao, M.; Jiang, L. A Multi-Bioinspired Dual-Gradient Electrode for Microbubble Manipulation toward Controllable Water Splitting. *Adv. Mater.* **2020**, *32*, e1908099. [[CrossRef](#)] [[PubMed](#)]
26. Hou, P.; Li, D.; Yang, N.; Wan, J.; Zhang, C.; Zhang, X.; Jiang, H.; Zhang, Q.; Gu, L.; Wang, D. Delicate Control on the Shell Structure of Hollow Spheres Enables Tunable Mass Transport in Water Splitting. *Angew. Chem. Int. Ed. Engl.* **2021**, *60*, 6926–6931. [[CrossRef](#)]
27. Zhang, F.; Zhao, R.; Wang, Y.; Han, L.; Gu, J.; Niu, Z.; Yuan, Y.; Qu, N.; Meng, J.; Wang, D. Superwettable Surface-Dependent efficiently electrocatalytic water splitting based on their excellent liquid adsorption and gas desorption. *Chem. Eng. J.* **2023**, *452*, 139513. [[CrossRef](#)]
28. Yuan, Y.; Pan, J.; Yin, W.; Yu, H.; Wang, F.; Hu, W.; Wang, L.; Yan, D. Effective strategies to promote Z(S)-scheme photocatalytic water splitting. *Chin. Chem. Lett.* **2024**, *35*, 108724. [[CrossRef](#)]
29. Hegner, K.I.; Wong, W.S.Y.; Vollmer, D. Ultrafast Bubble Bursting by Superamphiphobic Coatings. *Adv. Mater.* **2021**, *33*, e2101855. [[CrossRef](#)]
30. Li, X.; Zhang, J.; Wang, X.; Lv, D.; Cao, C.; Ai, L.; Yao, X. Bio-inspired spontaneous splitting of underwater bubbles along a superhydrophobic open pathway without perturbation. *Droplet* **2022**, *1*, 65–75. [[CrossRef](#)]
31. Qiao, S.; Cai, C.; Chen, W.; Pan, C.; Liu, Y. Control of the shape of bubble growth on underwater substrates with different sizes of superhydrophobic circles. *Phys. Fluids* **2022**, *34*, 067110. [[CrossRef](#)]
32. Yong, J.; Yang, Q.; Huo, J.; Hou, X.; Chen, F. Underwater gas self-transportation along femtosecond laser-written open superhydrophobic surface microchannels (<100 μm) for bubble/gas manipulation. *Int. J. Extreme Manuf.* **2022**, *4*, 015002. [[CrossRef](#)]
33. Shen, J.; Li, B.; Zheng, Y.; Dai, Z.; Li, J.; Bao, X.; Guo, J.; Yu, X.; Guo, Y.; Ge, M.; et al. Engineering the composition and structure of superaerophobic nanosheet array for efficient hydrogen evolution. *Chem. Eng. J.* **2022**, *433*, 133517. [[CrossRef](#)]
34. Jiao, Y.; Lv, X.; Zhang, Y.; Li, C.; Li, J.; Wu, H.; Xiao, Y.; Wu, S.; Hu, Y.; Wu, D.; et al. Pitcher plant-bioinspired bubble slippery surface fabricated by femtosecond laser for buoyancy-driven bubble self-transport and efficient gas capture. *Nanoscale* **2019**, *11*, 1370–1378. [[CrossRef](#)]
35. Zhang, Q.; Prokhorchenko, S.; Nahas, Y.; Xie, L.; Bellaiche, L.; Gruverman, A.; Valanoor, N. Deterministic Switching of Ferroelectric Bubble Nanodomains. *Adv. Funct. Mater.* **2019**, *29*, 1808573. [[CrossRef](#)]

36. Giacomello, A.; Roth, R. Bubble formation in nanopores: A matter of hydrophobicity, geometry, and size. *Adv. Phys. X* **2020**, *5*, 1817780. [[CrossRef](#)]
37. Tang, J.; Wu, Y.; Kong, L.; Wang, W.; Chen, Y.; Wang, Y.; Soh, Y.; Xiong, Y.; Tian, M.; Du, H. Two-dimensional characterization of three-dimensional magnetic bubbles in  $\text{Fe}_3\text{Sn}_2$  nanostructures. *Natl. Sci. Rev.* **2021**, *8*, nwaa200. [[CrossRef](#)]
38. Yin, K.; Yang, S.; Dong, X.; Chu, D.; Gong, X.; Duan, J.-A. Femtosecond laser fabrication of shape-gradient platform: Underwater bubbles continuous self-driven and unidirectional transportation. *Appl. Surf. Sci.* **2019**, *471*, 999–1004. [[CrossRef](#)]
39. Jeon, D.; Park, J.; Shin, C.; Kim, H.; Jang, J.W.; Lee, D.W.; Ryu, J. Superaerophobic hydrogels for enhanced electrochemical and photoelectrochemical hydrogen production. *Sci. Adv.* **2020**, *6*, eaaz3944. [[CrossRef](#)]
40. Zhang, C.; Xu, Z.; Han, N.; Tian, Y.; Kallio, T.; Yu, C.; Jiang, L. Superaerophilic/superaerophobic cooperative electrode for efficient hydrogen evolution reaction via enhanced mass transfer. *Sci. Adv.* **2023**, *9*, eadd6978. [[CrossRef](#)] [[PubMed](#)]
41. Li, J.; Yin, W.; Pan, J.; Zhang, Y.; Wang, F.; Wang, L.; Zhao, Q. External field assisted hydrogen evolution reaction. *Nano Res.* **2023**, *16*, 8638–8654. [[CrossRef](#)]
42. Dastafkan, K.; Meyer, Q.; Chen, X.; Zhao, C. Efficient Oxygen Evolution and Gas Bubble Release Achieved by a Low Gas Bubble Adhesive Iron-Nickel Vanadate Electrocatalyst. *Small* **2020**, *16*, e2002412. [[CrossRef](#)]
43. Shi, H.; Zhang, H.; Huo, D.; Yu, S.; Su, J.; Xie, Y.; Li, W.; Ma, L.; Chen, H.; Sun, Y. An Ultrasensitive Microsensor Based on Impedance Analysis for Oil Condition Monitoring. *IEEE Trans. Ind. Electron.* **2022**, *69*, 7441–7450. [[CrossRef](#)]
44. Lu, S.M.; Li, Y.J.; Zhang, J.F.; Wang, Y.; Ying, Y.L.; Long, Y.T. Monitoring Hydrogen Evolution Reaction Catalyzed by  $\text{MoS}_2$  Quantum Dots on a Single Nanoparticle Electrode. *Anal. Chem.* **2019**, *91*, 10361–10365. [[CrossRef](#)]
45. Liu, Y.; Jin, C.; Liu, Y.; Ruiz, K.H.; Ren, H.; Fan, Y.; White, H.S.; Chen, Q. Visualization and Quantification of Electrochemical  $\text{H}_2$  Bubble Nucleation at Pt, Au, and  $\text{MoS}_2$  Substrates. *ACS Sens.* **2021**, *6*, 355–363. [[CrossRef](#)]
46. Gao, Y.; Wu, M.; Lin, Y.; Xu, J. Trapping and control of bubbles in various microfluidic applications. *Lab Chip* **2020**, *20*, 4512–4527. [[CrossRef](#)] [[PubMed](#)]
47. Li, Y.; Liu, X.; Huang, Q.; Ohta, A.T.; Arai, T. Bubbles in microfluidics: An all-purpose tool for micromanipulation. *Lab Chip* **2021**, *21*, 1016–1035. [[CrossRef](#)]
48. Viejo, C.G.; Torrico, D.D.; Dunshea, F.R.; Fuentes, S. Bubbles, Foam Formation, Stability and Consumer Perception of Carbonated Drinks: A Review of Current, New and Emerging Technologies for Rapid Assessment and Control. *Foods* **2019**, *8*, 596. [[CrossRef](#)] [[PubMed](#)]
49. Lin, C.; Li, Z.; Lu, L.; Cai, S.; Maxey, M.; Karniadakis, G.E. Operator learning for predicting multiscale bubble growth dynamics. *J. Chem. Phys.* **2021**, *154*, 104118. [[CrossRef](#)]
50. Dastafkan, K.; Wang, S.; Rong, C.; Meyer, Q.; Li, Y.; Zhang, Q.; Zhao, C. Cosynergistic Molybdate Oxo-Anionic Modification of FeNi-Based Electrocatalysts for Efficient Oxygen Evolution Reaction. *Adv. Funct. Mater.* **2021**, *32*, 2107342. [[CrossRef](#)]
51. Dastafkan, K.; Wang, S.; Song, S.; Meyer, Q.; Zhang, Q.; Shen, Y.; Zhao, C. Operando monitoring of gas bubble evolution in water electrolysis by single high-frequency impedance. *EES Catal.* **2023**, *1*, 998–1008. [[CrossRef](#)]
52. Zhang, W.; Li, G.; Liu, H.; Chen, J.; Ma, S.; An, T. Micro/nano-bubble assisted synthesis of  $\text{Au}/\text{TiO}_2@\text{CNTs}$  composite photocatalyst for photocatalytic degradation of gaseous styrene and its enhanced catalytic mechanism. *Environ. Sci. Nano* **2019**, *6*, 948–958. [[CrossRef](#)]
53. Wang, Y.; Gordon, E.; Ren, H. Mapping the Nucleation of  $\text{H}_2$  Bubbles on Polycrystalline Pt via Scanning Electrochemical Cell Microscopy. *J. Phys. Chem. Lett.* **2019**, *10*, 3887–3892. [[CrossRef](#)]
54. Zhong, X.; Eshraghi, J.; Vlachos, P.; Dabiri, S.; Ardekani, A.M. A model for a laser-induced cavitation bubble. *Int. J. Multiph. Flow* **2020**, *132*, 103433. [[CrossRef](#)]
55. Song, C.; Jin, D.; Choi, S.; Lee, Y. Fiber-in-tube  $\text{RuCr}_{1-x}\text{O}_y$  as highly efficient electrocatalysts for pH-universal water oxidation via facile bubble desorption. *J. Mater. Chem. A* **2023**, *11*, 26626–26635. [[CrossRef](#)]
56. Wang, X.; Shuai, Y.; Zhang, H.; Sun, J.; Yang, Y.; Huang, Z.; Jiang, B.; Liao, Z.; Wang, J.; Yang, Y. Bubble breakup in a swirl-venturi microbubble generator. *Chem. Eng. J.* **2021**, *403*, 126397. [[CrossRef](#)]
57. Mosavi, A.; Shamshirband, S.; Salwana, E.; Chau, K.-W.; Tah, J.H.M. Prediction of multi-inputs bubble column reactor using a novel hybrid model of computational fluid dynamics and machine learning. *Eng. Appl. Comput. Fluid Mech.* **2019**, *13*, 482–492. [[CrossRef](#)]
58. Zhang, P.; Zhou, X.; Cheng, X.; Sun, H.; Ma, H.; Li, Y. Elucidation of bubble evolution and defect formation in directed energy deposition based on direct observation. *Addit. Manuf.* **2020**, *32*, 101026. [[CrossRef](#)]
59. Zhou, R.; Zhou, R.; Wang, P.; Luan, B.; Zhang, X.; Fang, Z.; Xian, Y.; Lu, X.; Ostrikov, K.K.; Bazaka, K. Microplasma Bubbles: Reactive Vehicles for Biofilm Dispersal. *ACS Appl. Mater. Interfaces* **2019**, *11*, 20660–20669. [[CrossRef](#)]
60. Sattari, A.; Hanafizadeh, P.; Hoofar, M. Multiphase flow in microfluidics: From droplets and bubbles to the encapsulated structures. *Adv. Colloid Interface Sci.* **2020**, *282*, 102208. [[CrossRef](#)]
61. Cherdantsev, A.V.; An, J.S.; Charogiannis, A.; Markides, C.N. Simultaneous application of two laser-induced fluorescence approaches for film thickness measurements in annular gas-liquid flows. *Int. J. Multiph. Flow* **2019**, *119*, 237–258. [[CrossRef](#)]
62. Zhu, J.; Zhu, H.; Zhang, J.; Zhang, H.-Q. A numerical study on flow patterns inside an electrical submersible pump (ESP) and comparison with visualization experiments. *J. Pet. Sci. Eng.* **2019**, *173*, 339–350. [[CrossRef](#)]
63. Gallo, M.; Magaletti, F.; Casciola, C.M. Heterogeneous bubble nucleation dynamics. *J. Fluid Mech.* **2020**, *906*, A20. [[CrossRef](#)]

64. Gallo, M.; Magaletti, F.; Cocco, D.; Casciola, C.M. Nucleation and growth dynamics of vapour bubbles. *J. Fluid Mech.* **2019**, *883*, A14. [[CrossRef](#)]
65. Scialdone, O.; Galia, A.; Sabatino, S. Electro-generation of H<sub>2</sub>O<sub>2</sub> and abatement of organic pollutant in water by an electro-Fenton process in a microfluidic reactor. *Electrochim. Commun.* **2013**, *26*, 45–47. [[CrossRef](#)]
66. Lu, Y.; Fu, T.; Zhu, C.; Ma, Y.; Li, H.Z. Pinch-off mechanism for Taylor bubble formation in a microfluidic flow-focusing device. *Microfluid. Nanofluid.* **2013**, *16*, 1047–1055. [[CrossRef](#)]
67. Swiegers, G.F.; Terrett, R.N.L.; Tsekouras, G.; Tsuzuki, T.; Pace, R.J.; Stranger, R. The prospects of developing a highly energy-efficient water electrolyser by eliminating or mitigating bubble effects. *Sustain. Energy Fuels* **2021**, *5*, 1280–1310. [[CrossRef](#)]
68. Xu, Y.; Ye, D.; Zhu, X.; Wang, Y.; Yang, Y.; Chen, R.; Li, J.; Liao, Q. Bubble dynamic behaviors in the anode porous transport layer of proton exchange membrane electrolyzers using a microfluidic reactor. *J. Power Sources* **2023**, *582*, 233532. [[CrossRef](#)]
69. Perez Sirkin, Y.A.; Gadea, E.D.; Scherlis, D.A.; Molinero, V. Mechanisms of Nucleation and Stationary States of Electrochemically Generated Nanobubbles. *J. Am. Chem. Soc.* **2019**, *141*, 10801–10811. [[CrossRef](#)] [[PubMed](#)]
70. Bar-Zion, A.; Nourmahnad, A.; Mittelstein, D.R.; Shivaei, S.; Yoo, S.; Buss, M.T.; Hurt, R.C.; Malounda, D.; Abedi, M.H.; Lee-Gosselin, A.; et al. Acoustically triggered mechanotherapy using genetically encoded gas vesicles. *Nat. Nanotechnol.* **2021**, *16*, 1403–1412. [[CrossRef](#)]
71. Zhu, Z.; Wang, D.; Yang, B.; Yin, W.; Ardkani, M.S.; Yao, J.; Drelich, J.W. Effect of nano-sized roughness on the flotation of magnesite particles and particle-bubble interactions. *Miner. Eng.* **2020**, *151*, 106340. [[CrossRef](#)]
72. Zhou, L.; Wang, S.; Zhang, L.; Hu, J. Generation and stability of bulk nanobubbles: A review and perspective. *Curr. Opin. Colloid Interface Sci.* **2021**, *53*, 101439. [[CrossRef](#)]
73. Yu, J.; Hu, K.; Zhang, Z.; Luo, L.; Liu, Y.; Zhou, D.; Wang, F.; Kuang, Y.; Xu, H.; Li, H.; et al. Interfacial nanobubbles' growth at the initial stage of electrocatalytic hydrogen evolution. *Energy Environ. Sci.* **2023**, *16*, 2068–2079. [[CrossRef](#)]
74. Morasch, M.; Liu, J.; Dirscherl, C.F.; Ianeselli, A.; Kuhnlein, A.; Le Vay, K.; Schwintek, P.; Islam, S.; Corpina, M.K.; Scheu, B.; et al. Heated gas bubbles enrich, crystallize, dry, phosphorylate and encapsulate prebiotic molecules. *Nat. Chem.* **2019**, *11*, 779–788. [[CrossRef](#)] [[PubMed](#)]
75. Xiao, X.; Zhang, C.; Ma, H.; Zhang, Y.; Liu, G.; Cao, M.; Yu, C.; Jiang, L. Bioinspired Slippery Cone for Controllable Manipulation of Gas Bubbles in Low-Surface-Tension Environment. *ACS Nano* **2019**, *13*, 4083–4090. [[CrossRef](#)]
76. Liu, W.; Li, N.; Weng, C.-s.; Huang, X.-l.; Kang, Y. Bubble dynamics and pressure field characteristics of underwater detonation gas jet generated by a detonation tube. *Phys. Fluids* **2021**, *33*, 023302. [[CrossRef](#)]
77. Cheng, H.; Long, X.; Ji, B.; Peng, X.; Farhat, M. A new Euler-Lagrangian cavitation model for tip-vortex cavitation with the effect of non-condensable gas. *Int. J. Multiph. Flow* **2021**, *134*, 103441. [[CrossRef](#)]
78. Rahimi, N.; Kang, D.; Gelinas, J.; Menon, A.; Gordon, M.J.; Metiu, H.; McFarland, E.W. Solid carbon production and recovery from high temperature methane pyrolysis in bubble columns containing molten metals and molten salts. *Carbon* **2019**, *151*, 181–191. [[CrossRef](#)]
79. Visser, C.W.; Amato, D.N.; Mueller, J.; Lewis, J.A. Architected Polymer Foams via Direct Bubble Writing. *Adv. Mater.* **2019**, *31*, e1904668. [[CrossRef](#)] [[PubMed](#)]
80. Yue, C.; Khater, M.M.A.; Attia, R.A.M.; Lu, D. The plethora of explicit solutions of the fractional KS equation through liquid–gas bubbles mix under the thermodynamic conditions via Atangana–Baleanu derivative operator. *Adv. Differ. Equ.* **2020**, *2020*, 62. [[CrossRef](#)]
81. Wang, J. Continuum theory for dense gas-solid flow: A state-of-the-art review. *Chem. Eng. Sci.* **2020**, *215*, 115428. [[CrossRef](#)]
82. Gordillo, J.M.; Rodríguez-Rodríguez, J. Capillary waves control the ejection of bubble bursting jets. *J. Fluid Mech.* **2019**, *867*, 556–571. [[CrossRef](#)]
83. Yang, H.Y.K.; Gaspari, M.; Marlow, C. The Impact of Radio AGN Bubble Composition on the Dynamics and Thermal Balance of the Intracluster Medium. *Astrophys. J.* **2019**, *871*, 6. [[CrossRef](#)]
84. Lechner, C.; Lauterborn, W.; Koch, M.; Mettin, R. Jet formation from bubbles near a solid boundary in a compressible liquid: Numerical study of distance dependence. *Phys. Rev. Fluids* **2020**, *5*, 093604. [[CrossRef](#)]
85. Park, S.; Liu, L.; Demirkir, C.; van der Heijden, O.; Lohse, D.; Krug, D.; Koper, M.T.M. Solutal Marangoni effect determines bubble dynamics during electrocatalytic hydrogen evolution. *Nat. Chem.* **2023**, *15*, 1532–1540. [[CrossRef](#)]
86. Gudkov, S.V.; Penkov, N.V.; Baimler, I.V.; Lyakhov, G.A.; Pustovoy, V.I.; Simakin, A.V.; Sarimov, R.M.; Scherbakov, I.A. Effect of Mechanical Shaking on the Physicochemical Properties of Aqueous Solutions. *Int. J. Mol. Sci.* **2020**, *21*, 8033. [[CrossRef](#)]
87. Ulseth, A.J.; Hall, R.O.; Boix Canadell, M.; Madinger, H.L.; Niayifar, A.; Battin, T.J. Distinct air–water gas exchange regimes in low- and high-energy streams. *Nat. Geosci.* **2019**, *12*, 259–263. [[CrossRef](#)]
88. Zhu, D.; Xu, L.; Su, X.; Hu, B.; Jia, T.; Mi, L. Experimental study of the effect of mechanical vibration and water velocity on bubble management in PEM electrolysis cell. *Int. J. Hydrogen Energy* **2023**, *49*, 390–403. [[CrossRef](#)]
89. Maier, M.; Meyer, Q.; Majasan, J.; Owen, R.E.; Robinson, J.B.; Dodwell, J.; Wu, Y.; Castanheira, L.; Hinds, G.; Shearing, P.R.; et al. Diagnosing Stagnant Gas Bubbles in a Polymer Electrolyte Membrane Water Electrolyser Using Acoustic Emission. *Front. Energy Res.* **2020**, *8*, 582919. [[CrossRef](#)]
90. Al Ramadan, M.; Salehi, S.; Kwiatka, G.; Ezeakacha, C.; Teodoriu, C. Experimental investigation of well integrity: Annular gas migration in cement column. *J. Pet. Sci. Eng.* **2019**, *179*, 126–135. [[CrossRef](#)]

91. Ye, L.; Zhu, X.; Liu, Y. Numerical study on dual-frequency ultrasonic enhancing cavitation effect based on bubble dynamic evolution. *Ultrason. Sonochem.* **2019**, *59*, 104744. [[CrossRef](#)]
92. Chu, H.; Yu, X.; Jiang, H.; Wang, D.; Xu, N. Progress in enhanced pool boiling heat transfer on macro- and micro-structured surfaces. *Int. J. Heat Mass Transf.* **2023**, *200*, 123530. [[CrossRef](#)]
93. Karimi, V.; Sharma, R.; Morgen, P.; Andersen, S.M. Multiple Bubble Removal Strategies to Promote Oxygen Evolution Reaction: Mechanistic Understandings from Orientation, Rotation, and Sonication Perspectives. *ACS Appl. Mater. Interfaces* **2023**, *15*, 49233–49245. [[CrossRef](#)]
94. Bae, M.; Kang, Y.; Lee, D.W.; Jeon, D.; Ryu, J. Superaerophobic Polyethyleneimine Hydrogels for Improving Electrochemical Hydrogen Production by Promoting Bubble Detachment. *Adv. Energy Mater.* **2022**, *12*, 2201452. [[CrossRef](#)]
95. Shan, X.; Liu, J.; Mu, H.; Xiao, Y.; Mei, B.; Liu, W.; Lin, G.; Jiang, Z.; Wen, L.; Jiang, L. An Engineered Superhydrophilic/Superaerophobic Electrocatalyst Composed of the Supported CoMoS(x) Chalcogel for Overall Water Splitting. *Angew. Chem. Int. Ed. Engl.* **2020**, *59*, 1659–1665. [[CrossRef](#)]
96. Andaveh, R.; Barati Darband, G.; Maleki, M.; Sabour Rouhaghdam, A. Superaerophobic/superhydrophilic surfaces as advanced electrocatalysts for the hydrogen evolution reaction: A comprehensive review. *J. Mater. Chem. A* **2022**, *10*, 5147–5173. [[CrossRef](#)]
97. Sun, H.; Yan, Z.; Liu, F.; Xu, W.; Cheng, F.; Chen, J. Self-Supported Transition-Metal-Based Electrocatalysts for Hydrogen and Oxygen Evolution. *Adv. Mater.* **2020**, *32*, e1806326. [[CrossRef](#)]
98. Dastafkan, K.; Li, Y.; Zeng, Y.; Han, L.; Zhao, C. Enhanced surface wettability and innate activity of an iron borate catalyst for efficient oxygen evolution and gas bubble detachment. *J. Mater. Chem. A* **2019**, *7*, 15252–15261. [[CrossRef](#)]
99. Xia, C.; Back, S.; Ringe, S.; Jiang, K.; Chen, F.; Sun, X.; Siahrostami, S.; Chan, K.; Wang, H. Confined local oxygen gas promotes electrochemical water oxidation to hydrogen peroxide. *Nat. Catal.* **2020**, *3*, 125–134. [[CrossRef](#)]
100. Shang, L.; Zhao, Y.; Kong, X.-Y.; Shi, R.; Waterhouse, G.I.N.; Wen, L.; Zhang, T. Underwater superaerophobic Ni nanoparticle-decorated nickel–molybdenum nitride nanowire arrays for hydrogen evolution in neutral media. *Nano Energy* **2020**, *78*, 105375. [[CrossRef](#)]
101. Hashemi, L.; Glerum, W.; Farajzadeh, R.; Hajibeygi, H. Contact angle measurement for hydrogen/brine/sandstone system using captive-bubble method relevant for underground hydrogen storage. *Adv. Water Resour.* **2021**, *154*, 103964. [[CrossRef](#)]
102. Zhang, Q.; Sun, D.; Pan, S.; Zhu, M. Microporosity formation and dendrite growth during solidification of aluminum alloys: Modeling and experiment. *Int. J. Heat Mass Transf.* **2020**, *146*, 118838. [[CrossRef](#)]
103. Iwata, R.; Zhang, L.; Wilke, K.L.; Gong, S.; He, M.; Gallant, B.M.; Wang, E.N. Bubble growth and departure modes on wettable/non-wettable porous foams in alkaline water splitting. *Joule* **2021**, *5*, 887–900. [[CrossRef](#)]
104. Shi, W.; Yang, X.; Sommerfeld, M.; Yang, J.; Cai, X.; Li, G.; Zong, Y. Modelling of mass transfer for gas-liquid two-phase flow in bubble column reactor with a bubble breakage model considering bubble-induced turbulence. *Chem. Eng. J.* **2019**, *371*, 470–485. [[CrossRef](#)]
105. Liu, R.; Gong, Z.; Liu, J.; Dong, J.; Liao, J.; Liu, H.; Huang, H.; Liu, J.; Yan, M.; Huang, K.; et al. Design of Aligned Porous Carbon Films with Single-Atom Co-N-C Sites for High-Current-Density Hydrogen Generation. *Adv. Mater.* **2021**, *33*, e2103533. [[CrossRef](#)] [[PubMed](#)]
106. Zhang, D.; Ranjan, B.; Tanaka, T.; Sugioka, K. Underwater persistent bubble-assisted femtosecond laser ablation for hierarchical micro/nanostructuring. *Int. J. Extreme Manuf.* **2020**, *2*, 015001. [[CrossRef](#)]
107. Yin, W.; Cai, Y.; Xie, L.; Huang, H.; Zhu, E.; Pan, J.; Bu, J.; Chen, H.; Yuan, Y.; Zhuang, Z.; et al. Revisited electrochemical gas evolution reactions from the perspective of gas bubbles. *Nano Res.* **2022**, *16*, 4381–4398. [[CrossRef](#)]
108. Li, M.; Yin, W.; Pan, J.; Zhu, Y.; Sun, N.; Zhang, X.; Wan, Y.; Luo, Z.; Yi, L.; Wang, L. Hydrogen spillover as a promising strategy for boosting heterogeneous catalysis and hydrogen storage. *Chem. Eng. J.* **2023**, *471*, 144691. [[CrossRef](#)]
109. He, S.; Wang, K.; Li, B.; Du, H.; Du, Z.; Wang, T.; Li, S.; Ai, W.; Huang, W. The Secret of Nanoarrays toward Efficient Electrochemical Water Splitting: A Vision of Self-Dynamic Electrolyte. *Adv. Mater.* **2023**, *35*, e2307017. [[CrossRef](#)] [[PubMed](#)]
110. Ren, Q.; Feng, L.; Ye, C.; Xue, X.; Lin, D.; Eisenberg, S.; Kou, T.; Duoss, E.B.; Zhu, C.; Li, Y. Nanocone-Modified Surface Facilitates Gas Bubble Detachment for High-Rate Alkaline Water Splitting. *Adv. Energy Mater.* **2023**, *13*, 2302073. [[CrossRef](#)]
111. Wang, J.; Liang, C.; Ma, X.; Liu, P.; Pan, W.; Zhu, H.; Guo, Z.; Sui, Y.; Liu, H.; Liu, L.; et al. Dynamically Adaptive Bubbling for Upgrading Oxygen Evolution Reaction Using Lamellar Fern-Like Alloy Aerogel Self-Standing Electrodes. *Adv. Mater.* **2023**, *36*, e2307925. [[CrossRef](#)] [[PubMed](#)]
112. Du, H.; Wang, T.; He, S.; Li, B.; Wang, K.; Chen, Q.; Du, Z.; Ai, W.; Huang, W. Mountain-Shaped Nickel Nanostripes Enabled by Facet Engineering of Nickel Foam: A New Platform for High-Current-Density Water Splitting. *Adv. Funct. Mater.* **2023**, *34*, 2311854. [[CrossRef](#)]
113. Kim, J.; Jung, S.M.; Lee, N.; Kim, K.S.; Kim, Y.T.; Kim, J.K. Efficient Alkaline Hydrogen Evolution Reaction Using Superaerophobic Ni Nanoarrays with Accelerated H<sub>2</sub> Bubble Release. *Adv. Mater.* **2023**, *35*, e2305844. [[CrossRef](#)]
114. Yu, X.; Yu, Z.Y.; Zhang, X.L.; Zheng, Y.R.; Duan, Y.; Gao, Q.; Wu, R.; Sun, B.; Gao, M.R.; Wang, G.; et al. “Superaerophobic” Nickel Phosphide Nanoarray Catalyst for Efficient Hydrogen Evolution at Ultrahigh Current Densities. *J. Am. Chem. Soc.* **2019**, *141*, 7537–7543. [[CrossRef](#)] [[PubMed](#)]
115. Yin, W.; Yuan, L.; Huang, H.; Cai, Y.; Pan, J.; Sun, N.; Zhang, Q.; Shu, Q.; Gu, C.; Zhuang, Z.; et al. Strategies to accelerate bubble detachment for efficient hydrogen evolution. *Chin. Chem. Lett.* **2024**, *35*, 108351. [[CrossRef](#)]

116. Tan, B.H.; An, H.; Ohl, C.-D. Stability of surface and bulk nanobubbles. *Curr. Opin. Colloid Interface Sci.* **2021**, *53*, 101428. [[CrossRef](#)]
117. Xie, L.; Wang, L.; Liu, X.; Zhao, W.; Liu, S.; Huang, X.; Zhao, Q. Tetra-Coordinated W<sub>2</sub>S<sub>3</sub> for Efficient Dual-pH Hydrogen Production. *Angew. Chem. Int. Ed. Engl.* **2024**, *63*, e202316306. [[CrossRef](#)]
118. Liu, H.; Xie, R.; Luo, Y.; Cui, Z.; Yu, Q.; Gao, Z.; Zhang, Z.; Yang, F.; Kang, X.; Ge, S.; et al. Dual interfacial engineering of a Chevrel phase electrode material for stable hydrogen evolution at 2500 mA cm<sup>-2</sup>. *Nat. Commun.* **2022**, *13*, 6382. [[CrossRef](#)]
119. Wang, L.; Zhang, F.; Sun, N.; Xie, L.; Zhi, T.; Zhang, Q.; Luo, Z.; Liu, X.; Liu, S.; Zhao, Q. Boosting hydrogen evolution on MoS<sub>2</sub> via synergistic regulation of interlayer dislocations and interlayer spacing. *Chem. Eng. J.* **2023**, *474*, 145792. [[CrossRef](#)]
120. Obayashi, I.; Nakamura, T.; Hiraoka, Y. Persistent Homology Analysis for Materials Research and Persistent Homology Software: HomCloud. *J. Phys. Soc. Jpn.* **2022**, *91*, 091013. [[CrossRef](#)]
121. Guo, X.; Zhang, C.; Tian, Q.; Yu, D. Liquid metals dealloying as a general approach for the selective extraction of metals and the fabrication of nanoporous metals: A review. *Mater. Today Commun.* **2021**, *26*, 102007. [[CrossRef](#)]
122. He, L.; Wang, H.; Chen, L.; Wang, X.; Xie, H.; Jiang, C.; Li, C.; Elibol, K.; Meyer, J.; Watanabe, K.; et al. Isolating hydrogen in hexagonal boron nitride bubbles by a plasma treatment. *Nat. Commun.* **2019**, *10*, 2815. [[CrossRef](#)]
123. Hu, S.; Setyawan, W.; Beeler, B.W.; Gan, J.; Burkes, D.E. Defect cluster and nonequilibrium gas bubble associated growth in irradiated UMo fuels—A cluster dynamics and phase field model. *J. Nucl. Mater.* **2020**, *542*, 152441. [[CrossRef](#)]
124. Lin, X.; Wang, Z.; Cao, S.; Hu, Y.; Liu, S.; Chen, X.; Chen, H.; Zhang, X.; Wei, S.; Xu, H.; et al. Bioinspired trimesic acid anchored electrocatalysts with unique static and dynamic compatibility for enhanced water oxidation. *Nat. Commun.* **2023**, *14*, 6714. [[CrossRef](#)]
125. Xie, L.; Wang, L.; Zhao, W.; Liu, S.; Huang, W.; Zhao, Q. WS<sub>2</sub> moire superlattices derived from mechanical flexibility for hydrogen evolution reaction. *Nat. Commun.* **2021**, *12*, 5070. [[CrossRef](#)] [[PubMed](#)]
126. MacLeod, J. Design and construction of on-surface molecular nanoarchitectures: Lessons and trends from trimesic acid and other small carboxylated building blocks. *J. Phys. D Appl. Phys.* **2020**, *53*, 043002. [[CrossRef](#)]
127. Xin, L.; Hu, J.; Wu, X.; Huang, K.; Huang, X. Fenton-like degradation of carmine dyes based on artificial intelligence modeling and optimization of reduced graphene oxide loaded iron-cobalt-nickel trimetallic nanocomposites. *Mater. Today Commun.* **2022**, *31*, 103463. [[CrossRef](#)]
128. Kou, T.; Wang, S.; Shi, R.; Zhang, T.; Chiovoloni, S.; Lu, J.Q.; Chen, W.; Worsley, M.A.; Wood, B.C.; Baker, S.E.; et al. Periodic Porous 3D Electrodes Mitigate Gas Bubble Traffic during Alkaline Water Electrolysis at High Current Densities. *Adv. Energy Mater.* **2020**, *10*, 2002955. [[CrossRef](#)]
129. Kim, Y.J.; Lim, A.; Kim, J.M.; Lim, D.; Chae, K.H.; Cho, E.N.; Han, H.J.; Jeon, K.U.; Kim, M.; Lee, G.H.; et al. Highly efficient oxygen evolution reaction via facile bubble transport realized by three-dimensionally stack-printed catalysts. *Nat. Commun.* **2020**, *11*, 4921. [[CrossRef](#)]
130. Liu, Z.; Du, Y.; Yu, R.; Zheng, M.; Hu, R.; Wu, J.; Xia, Y.; Zhuang, Z.; Wang, D. Tuning Mass Transport in Electrocatalysis Down to Sub-5 nm through Nanoscale Grade Separation. *Angew. Chem. Int. Ed. Engl.* **2023**, *62*, e202212653. [[CrossRef](#)] [[PubMed](#)]
131. Huang, X.; Liu, H.; Lu, D.; Lin, Y.; Liu, J.; Liu, Q.; Nie, Z.; Jiang, G. Mass spectrometry for multi-dimensional characterization of natural and synthetic materials at the nanoscale. *Chem. Soc. Rev.* **2021**, *50*, 5243–5280. [[CrossRef](#)] [[PubMed](#)]

**Disclaimer/Publisher’s Note:** The statements, opinions and data contained in all publications are solely those of the individual author(s) and contributor(s) and not of MDPI and/or the editor(s). MDPI and/or the editor(s) disclaim responsibility for any injury to people or property resulting from any ideas, methods, instructions or products referred to in the content.